EFFECTS OF ARTICULAR CARTILAGE DEFECT SIZE AND SHAPE ON SUBCHONDRAL BONE CONTACT: IMPLICATIONS FOR SURGICAL CARTILAGE RESTORATION

An Undergraduate Honors Thesis
Submitted to the Department of Mechanical Engineering
The Ohio State University
In Partial Fulfillment of the Requirements
For Graduation with Distinction in Mechanical Engineering

Peter Macy Brockmeier
May, 2008

ABSTRACT

Osteoarthritis (OA) progression involves the deterioration of articular cartilage, which, without surgical intervention, will not spontaneously stop. A number of factors influence this progression, two of which are cartilage defect size and subchondral bone changes that occur, such as sclerosis. Microfracture surgery generates mechanically inferior fibrocartilage repair tissue and succeeds in stopping OA progression in small defects, while ACI produces highly organized hyaline-like cartilage that has been shown to restore function and stop OA progression in large defects. The most frequently quoted threshold size to guide defect management is 2 cm^2 although there is relatively little clinical or biomechanical data to support this. Therefore, the purpose of this project was to determine the effect of defect size and shape on subchondral bone contact. Experimental biomechanical loading on bovine knees was preformed and defect subchondral bone contact was measured for defects ranging from 5 mm to 25 mm in diameter. Defect shape was also examined using oval – shaped defect. Results indicate that the current 2 cm^2 threshold for guiding management of articular cartilage defects may be too conservative, as major subchondral bone contact was not realized in defects below 2.87 cm^2 in our study. Furthermore, it was determined that subchondral bone contact was consistently higher in defect on the lateral condyle compared to that of the medial condyle. Preliminary testing of oval defect also suggests that the medial to lateral width of a defect may be more important than the absolute widest dimension of the defect.

ACKNOWLEDGEMENTS

I would first of all like to thank my advisor, Dr. Rob Siston. He was always willing to sit down with me and discuss the project, brainstorm ideas, or hold lengthy conversations over email. I now believe him that experimental research is a nasty animal, and that things rarely go the way you expect, but you just have to keep going with it.

I would like to thank Dr. Josh Harris for joining me for all of those 8-hour days in the lab completing testing. Also, I really appreciated all the page-long like emails explaining difficult concepts that seems so much more confusing in books and journal articles.

The project would not have existed without Dr. David Flanigan's numerous great ideas. It was always encouraging to me, as an undergraduate student, to see his enthusiasm about this study knowing that he had so many other interesting and important things going on.

I want thank Dr. Alan Litsky for being so generous in giving us time in the Orthopaedic Biomaterials Lab, and for his own time as well. He was always willing to make an extra trip to Davis Medical Research Center to unlock a door or prepare the lab for us.

And finally, I thank my wonderful girlfriend of three years, Tara Harrington, for being so understanding, especially during the last quarter of the project. Her support, advice, calming words, encouragement, and the example of unyielding perseverance in her own life honestly kept me sane and excited about this project.

TABLE OF CONTENTS

LIST OF FIGURES

LIST OF TABLES

Chapter 1: Introduction

1.1 Mechanical and Biological Properties of Articular Cartilage

The knee is arguably the most mechanically demanding of the synovial joints in humans due to the large compressive forces and complex motion between the femur and tibia. Experimental and mathematical studies of in vivo knee mechanics during various activities have shown that forces in the knee can regularly reach 2.5 times body weight, and during physical activity these forces can be upwards of 4 times body weight (Komistek et al., 2005). The complex forces, rotation, and translation at the tibio-femoral joint demand smooth and durable opposing surfaces capable of resisting compression. Articular cartilage, the thin material that covers the contacting femoral head and tibial plateau, provides these properties. When loaded, the opposing articular cartilage surfaces contact and compress and deform, distributing the applied force. Furthermore, a surrounding capsule called the synovium serves to contain a lubricating fluid within the joint that also is important for transporting nutrients throughout the joint. Healthy articular cartilage of the knee repeatedly provides a load bearing surface, force distribution, and a lubricated surface for articulation while experiencing virtually no wear (Setton et al., 1999).

As is the case with many biological materials, the macroscopic properties of articular cartilage can be attributed directly to its molecular structure and interactions. From a mechanical point of view, the three functions described above, load bearing, force distribution, and near-frictionless articulation, are related to the cartilage constituents and their organization and interaction. Articular cartilage is a complex composite material made up of a solid matrix saturated with a water phase. Both phases play important roles in giving

articular cartilage its mechanical properties. A mesh of collagen type II fibers entangled with large, aggregated proteoglycan molecules makes up the solid matrix, with the collagen fibers accounting for roughly 75% of the solid matrix by dry weight (Setton et al., 1999). The water phase, which includes sparsely suspended cartilage cells called chondrocytes, surrounds the solid matrix and accounts for roughly 65% to 80% of the total weight of the tissue (Figure 1) (Mandelbaum et al., 1998).

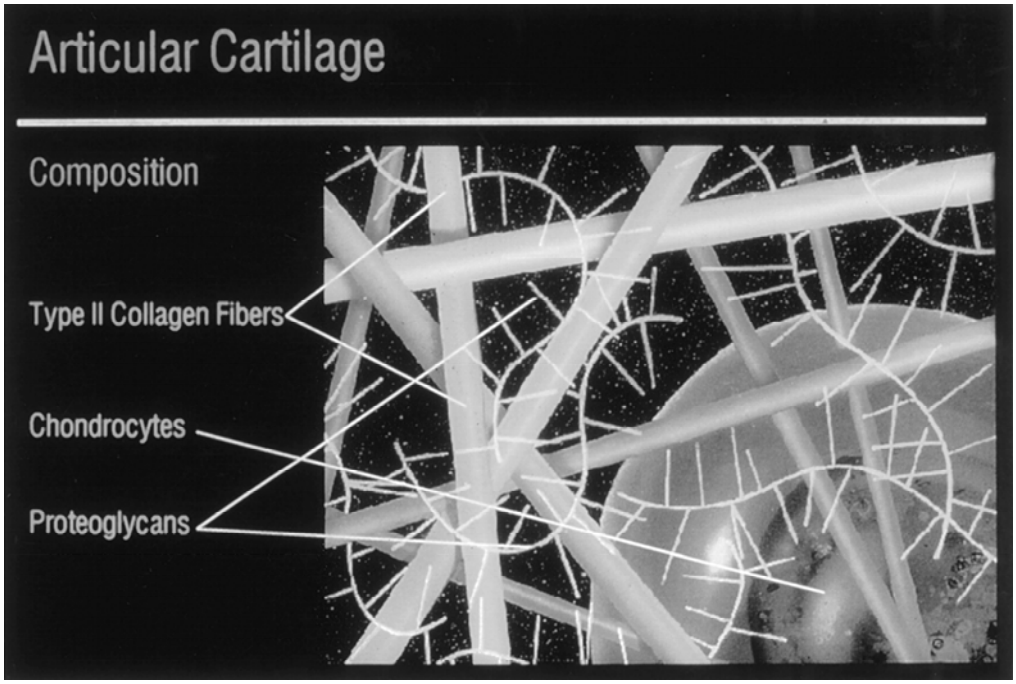

Figure 1: Composition of articular cartilage
Articular cartilage is a lattice-like structure composed of collagen fibers entangled with proteoglycans as a solid matrix, surrounded by water and suspended chondrocytes. From Mandelbaum et al., 1998.

The aggregated proteoglycan molecules, called aggrecan, contain negatively charged sulfate and carboxyl groups and thus impart a net negative charge on the solid matrix. The cartilage is thus hydrophilic, attracting exterior water molecules to traverse the semi-permeable cartilage surface to maintain electro-neutrality and causing the cartilage extracellular matrix to swell. The tendency to swell and expand the solid matrix in turn places the mesh of collagen fibers in tension (Maroudas, 1976). The result of these

combined effects is a large swelling pressure within the cartilage, giving it superb resistance to compression.

In addition to being biphasic, articular cartilage is comprised of four layers or zones, identifiable by the different orientation of or both collagen fibers (Figure 2) and chondrocytes (Figure 3). The upper 10% to 20%, including the surface, is the superficial tangential zone. In this zone, the collagen content is greatest and the fibers are oriented parallel to the joint surface, which facilitates sliding. Deep to the superficial zone is the middle zone, in which the collagen fibers are oriented randomly and chondrocytes are spherical. In the deep zone, collagen fibers are oriented perpendicular to the surface and have large diameter. Chondrocytes similarly are arranged in columns perpendicular to the surface in the deep zone (Flik et al., 2007). The calcified cartilage zone is separated from the deep zone by the tidemark and is the transition from cartilage to subchondral bone (SCB) (Flik et al., 2007; Mandelbaum et al., 1998). Subchondral bone is the division between cartilage and the cortical and trabelcular bone that makes up long bones.

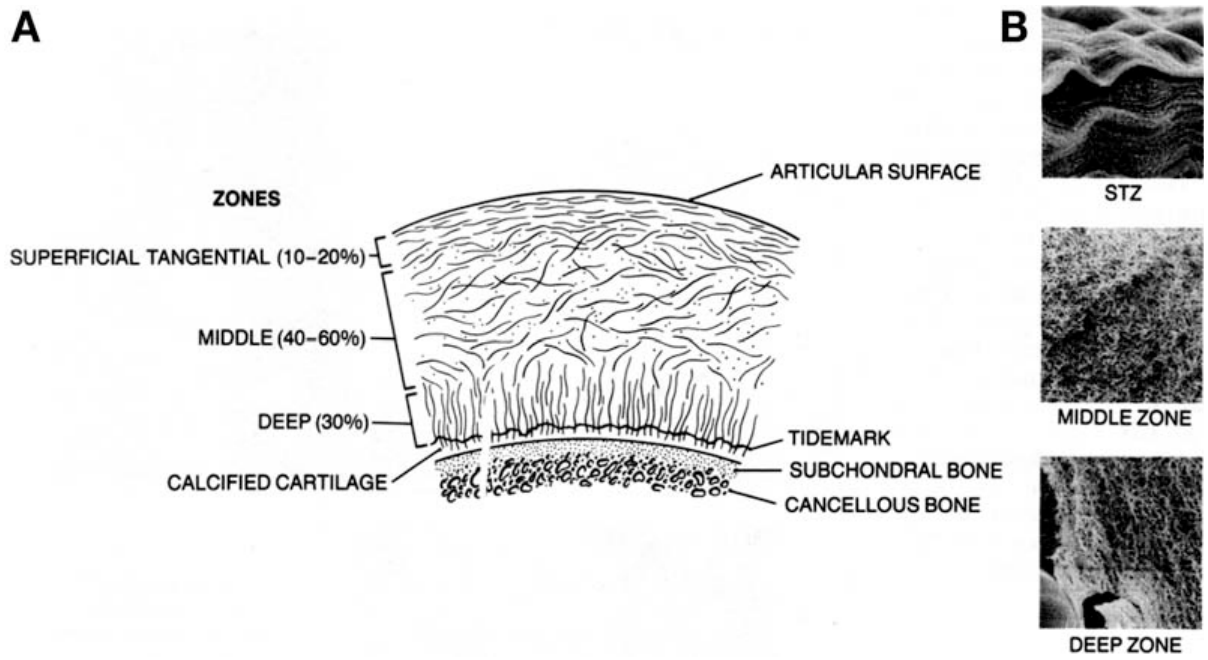

Figure 2: Collagen orientation in the four zones of articular cartilage
(A) Schematic drawing and (B) scanning electron micrographs. Collagen fibers are oriented parallel to the surface in the STZ, oriented randomly in the middle zone, and oriented perpendicular to the surface in the deep zone. From Flik et al., 2007.

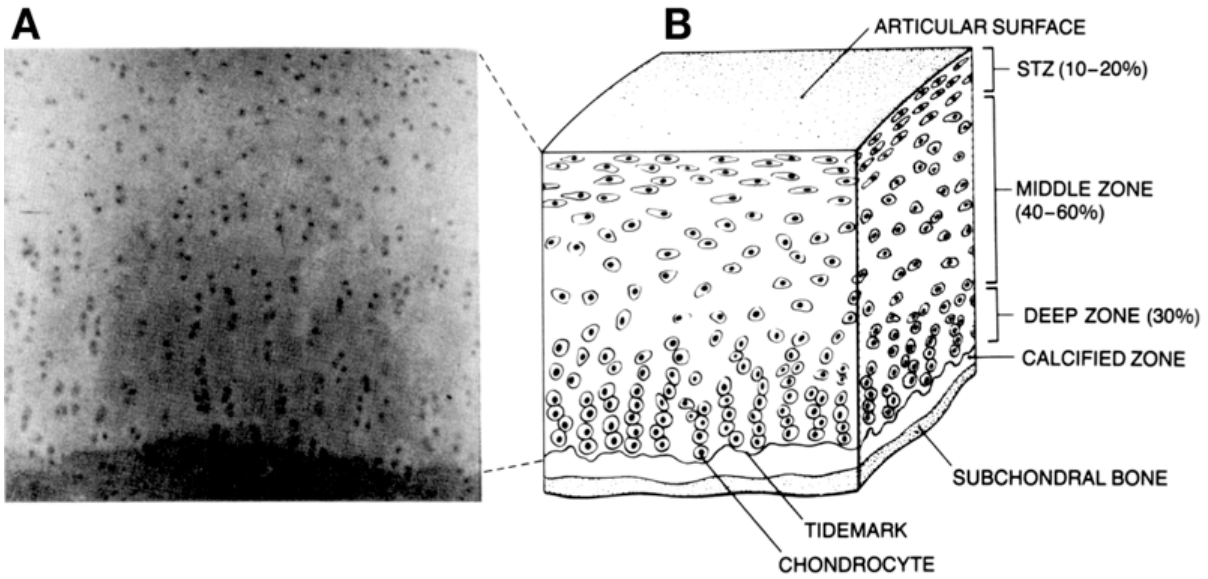

Figure 3: Chondrocyte orientation in the four zones of articular cartilage
(A) Histological image and (B) schematic drawing. Chondrocytes are ellipsoidal and lie parallel to the surface in the STZ, spherical in the middle zone, and spherical and aligned in columns perpendicular to the surface in the deep zone. From Flik et al., 2007.

Another important mechanical property of cartilage is its tendency to be viscoelastic. This is a product of the porosity of the cartilage and the large amount of water, which results in fluid flow when loaded. When loaded at different speeds, the mechanical properties vary drastically. For example, experimental studies have reported the elastic modulus of articular cartilage to be a few MPa at low loading rates, while the modulus can be near 500 MPa when loaded at dynamically to represent physiological loads (Radin et al., 1970).

Healthy cartilage is both aneural and avascular. Because it lacks nerves, one does not have sensation of pressure or rubbing that can occur in areas that contain nerves. This is largely advantageous, since substantial compressive and shear stresses occur in the joint. The lack of a vasculature is both advantageous and troublesome. In one respect, there are no blood vessels that would otherwise be damaged in the mechanically stressful environment of a knee joint. In fact, the hydrostatic pressure within articular cartilage inhibits vascular invasion from the underlying bone (Carter, 1987). However, blood carries important nutrients and reparative agents that would be beneficial to the upkeep of cartilage. The porosity of cartilage allows some nutrients to diffuse across the surface from the outer synovial fluid into the cartilage. These nutrients fuel the metabolically active chondrocytes, which maintain cartilage by balancing degradation and synthesis of proteoglycan, collagen, and other bio-macromolecules (Flik et al., 2007). This maintenance is limited by the low metabolic activity of chondrocytes, and therefore articular cartilage has a relatively poor ability to heal.

1.2 Osteoarthritis and Articular Cartilage Defects

Though articular cartilage is extremely durable and somewhat self-repairing,

degeneration of the tissue often occurs in the form of full- or partial-thickness loss of cartilage, the hallmark of degenerative osteoarthritis (Garnero et al., 2002). Osteoarthritis has generally been defined as the degeneration of articular cartilage and the formation of new bone at the joint surface and while the term "arthritis" implies some sort of inflammation, osteoarthritis is generally considered to be a non-inflammatory disorder (Attur et al., 2002). The exact cause of degenerative osteoarthritis is still unknown, although it has been suggested that an imbalance in the equilibrium between synthesis and degradation of articular cartilage by chondrocytes may be the first step (Attur et al., 2002; Garnero et al., 2002). It is generally accepted, though, that the degradation occurs in two phases. The first is the biosynthetic phase, in which chondrocytes attempt to repair the damaged extracellular matrix over time. Subsequently, a degradative phase occurs, in which enzymes produced by the chondrocytes digest the matrix, causing erosion of the cartilage (Sandell and Aigner, 2001). Osteoarthritis can be considered a natural occurrence that is unavoidable as aging occurs. It is estimated that 32 to 37 million Americans suffer from articular cartilage defects due to osteoarthritis (Steadman et al., 2001) and that 25 – 37% of people over 50 years of age suffer from osteoarthritis (Peat et al., 2006). It is also the leading cause of impaired mobility in the elderly (Felson, 2006).

In addition to degenerative osteoarthritis, trauma is a source of articular cartilage defects that occur most often in the knees of young and active people. In normal joints, mild to moderate activity is not likely to cause osteoarthritis. Those participating in collision sports, characterized by high-loading and torsional impacts, are at a higher risk for developing osteoarthritis (Hinton et al., 2002). For example, blunt impacts to articular cartilage have been found to result in immediate cell death (Bush et al., 2005; Duda et al.,

2001). The source of degradation in these cases is different than in normal osteoarthritis, but the resulting degeneration is similar.

Cartilage defects occur at different degrees of severity and vary in both depth and area. In general, scaling systems rank defects from minor softening and swelling to full thickness osteochondral defects. The standard grading system was developed by Outerbridge in 1961 and is defined as follows: grade 0, normal cartilage; grade I, cartilage with softening and swelling; grade II, partial thickness defect with fissures on the surface that do not reach SCB; grade III, fissuring to the level of SCB in an area with a diameter larger than 1.5 cm; grade IV, exposed SCB (Cameron et al., 2003).

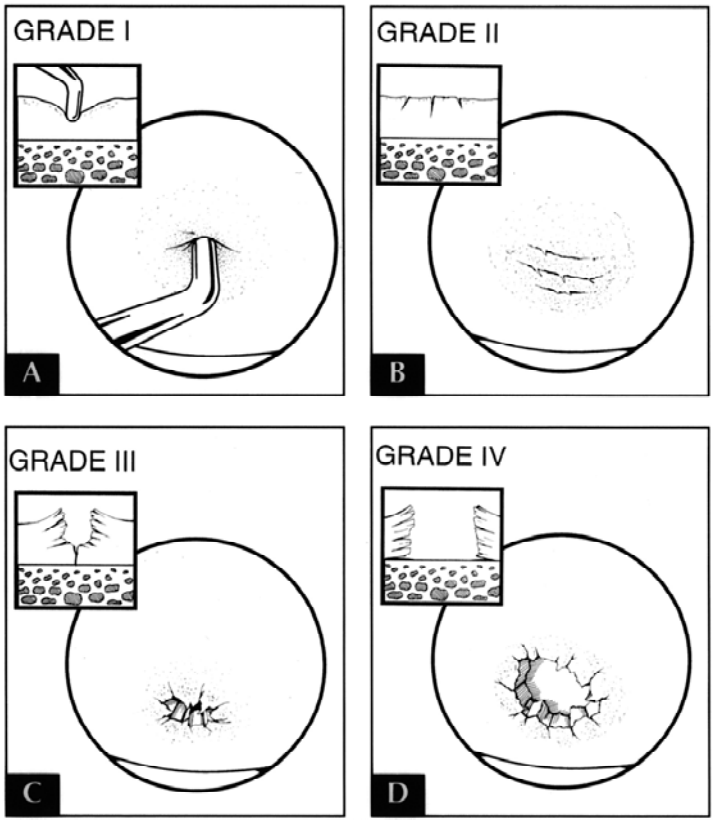

Figure 4: Outerbridge cartilage grading system

(A) Grade 1, cartilage with softening and swelling; (B) Grade II, partial thickness defect with fissures on the surface that do not reach SCB; (C) Grade III, fissuring to the level of SCB in an area with a diameter larger than 1.5 cm; (D) Grade IV, exposed SCB. Not included is a Grade 0 defect, which is normal cartilage. From (Mandelbaum et al., 1998).

Osteoarthritis is usually identified by radiographic means or clinical assessment by a physical examination of the joint (Peat et al., 2006). The usual primary symptom of osteoarthritis in the knee is simply pain in the joint. Also, global joint stiffness often occurs with moderate activity and after long periods of the knee being immobile. Prolonged joint stiffness and joint enlargement from swelling are signs of progression of osteoarthritis. As the disease becomes worse, a grating sensation in the joint is usually evident. In extreme cases, joint movement may be affected due to flexion contractures and mechanical obstructions. While the symptoms of articular cartilage defects do not always correlate with radiologic diagnoses, radiographs are effective in providing a more objective diagnosis following a physical examination (Hinton et al., 2002). A more precise diagnosis can be made with the use noninvasive cartilage-specific magnetic resonance imaging (MRI) (Sgaglione et al., 2002). Both x-rays and MRI diagnoses, unlike a physical examination, can help to determine the features of a defect that have been shown to be important in prescribing a successful repair procedure.

1.3 Repair Techniques

The features that generally guide surgical decisions are defect size (area), thickness, and location, all of which are determined by imaging techniques. Once information regarding the defect has been obtained, there are a number of surgical techniques that are available to relieve the pain and disabling effects of the defect. Procedures range from palliative, in which pain relief is the main objective, to restorative, in which the goal is to restore function completely (Figure 5) (Lewis et al., 2006).

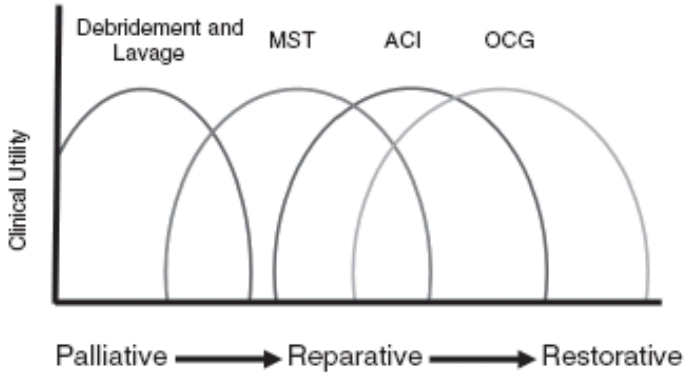

Figure 5: Clinical utility vs. procedure objectives
MST is marrow stimulation (such as microfracture), ACI is autologous chondrocyte implantation, and OCG is osteochondral grafting. The large overlap of marrow stimulation and ACI should be noted, as the treatments utilize similar healing procedures. From (Lewis et al., 2006).

1.3.1 Lavage and Debridement

Lavage and debridement are minor arthroscopic procedures that simply remove fragmented cartilage within the joint and clean up fibrillated cartilage, respectively, which combined can provide effective pain relief (Gill et al., 2006; Lewis et al., 2006). In practice, debridement would come first and involves the smoothing of fibrillated articular surfaces. Then lavage takes place, which washes away cartilage and bone fragments within the joint space. These procedures provide an initial solution but are not generally pursued as long term solutions or for patients desiring an active lifestyle following the surgery (Lewis et al., 2006).

1.3.2 Substitution Replacement

While lavage and debridement simply remove damaged cartilage from the injured knee, procedures have been developed that utilize a substitution replacement approach. Structures, generally cylindrical plugs, are inserted into a hole drilled into the condyle at the site of the defect. There are three options for the source of the plug. The most common

technique is osteochondral autograft transplantation, in which a cylindrical plug is removed from a healthy, minimally weight-bearing region of the patient knee and is then placed in the defect region where a hole of a slightly smaller diameter has been created (Lewis et al., 2006) (Figure 6).

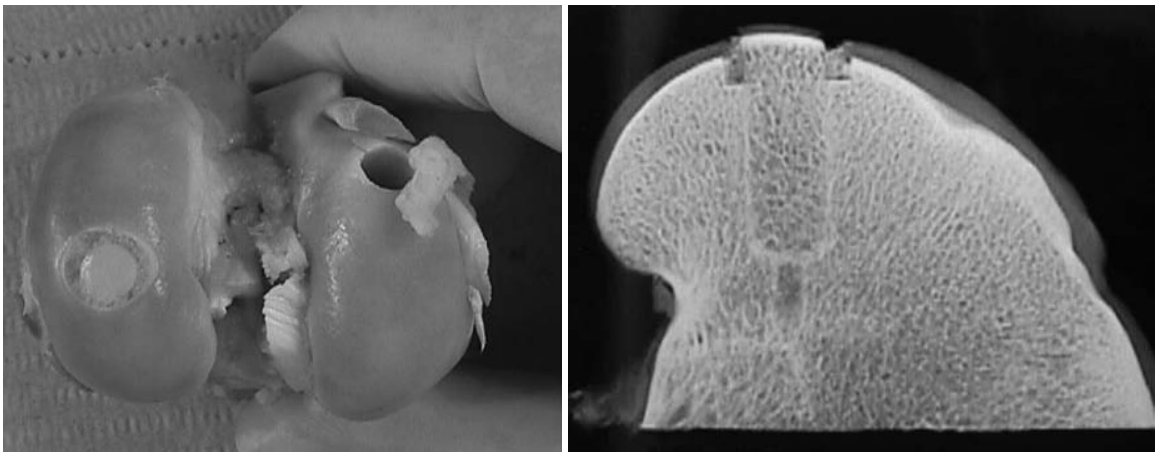

Figure 6: Images of osteochondral plug in the distal femur of a sheep
Left - view of plug (left condyle) and donor site (right condyle); Right - radiograph of lateral cross section. (Burks et al., 2006).

The plug, which is comprised of bone and cartilage from the patient, is press-fit into the hole so that the cartilage surface is flush with the surrounding surface. When the plug is removed from a cadaver knee, the procedure is called osteochondral allograft transplantation. In a successful osteochondral grafting procedure, the graft will be completely integrated with the adjacent bone and cartilage (Lewis et al., 2006). Multiple plugs are sometimes used in a procedure called mosaicplasty, in which a larger defect is filled in with a number of smaller plugs, with the interstices eventually becoming filled with fibrocartilage (Mandelbaum et al., 1998).

1.3.3 Regenerative or Restorative Procedures

Recently, interest in cartilage regeneration or restoration has increased as an alternative to replacement. Rather than replacing damaged cartilage with existing healthy

cartilage from the patient or a cadaver, regenerative procedures attempt to create new cartilage to fill in a defect. The first of these procedures, abrasion arthroplasty, was introduced and popularized over 20 years ago (Johnson, 1986). Because there is no vasculature within the cartilage, and a blood supply exists deep to the subchondral surface, the procedure involved the complete removal of the SCB plate layer using a scraping technique. Non-uniform repair tissue was often the result (Johnson, 2001). Later, a motorized procedure was developed, in which a spinning burr was used to remove the superficial bone layer. However, the procedure often resulted in the development of fibrocartilage generation, and in many cases the integrity of the SCB plate was sacrificed, eventually resulting in malalignment of the joint (Johnson, 2001).

1.3.4 Microfracture Surgery

The microfracture surgery was developed by Steadman in the 1980s (Steadman et al., 2001). The procedure attempts to take advantage of the pluripotency of mesenchymal stem cells (MSCs), which naturally reside within the marrow of the femur, to gradually regenerate new articular cartilage in a defect. The procedure is as follows: after a diagnosis has been performed and cartilage defects have been identified, a surgeon enters the knee arthroscopically and examines the defect region. The defect surface and edges are debrided, removing any damaged or loose cartilage. This step of the procedure has been found to be important in leading to a successful healing process (Steadman et al., 2001). The rim edge must be made as perpendicular as possible to contain the pre-cartilage material that eventually results (Figure 7). Failure to create a defect shouldered by intact cartilage leads pain and eventual progression of the defect (Yen et al., 2008).

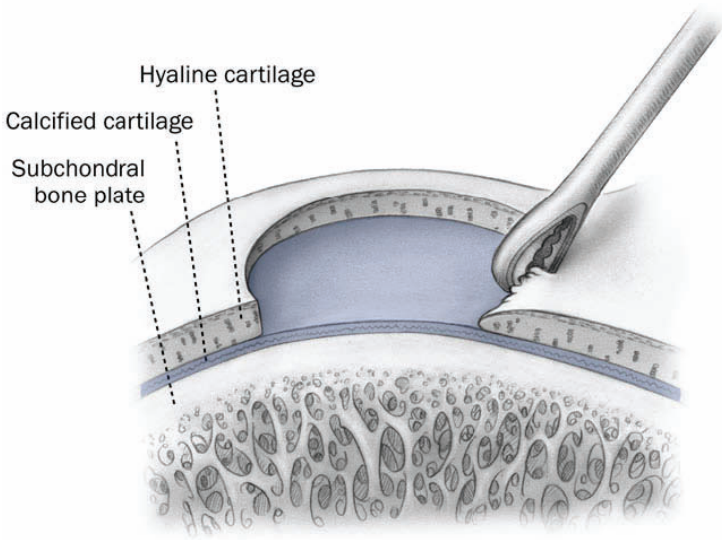

Figure 7: Microfracture surgery preparation
Drawing shows the use of a curette to create a stable rim of healthy adjacent cartilage. From (Mithoefer et al., 2006).

Then, the calcified cartilage layer, just superior to the SCB, is removed using a curette. A special tool resembling a small ice pick called an arthroscopic awl is then used manually to create multiple holes in the bone surface (Steadman et al., 2001). The holes, which should be placed 1-2 mm (Gill et al., 2006) or 3-4 mm (Gill et al., 2006; Mithoefer et al., 2006; Steadman et al., 2001) apart (Figure 8), serve as both the source of pre-cartilage material from within the SCB as well as a rough surface that leads to better adherence of this material (Gill et al., 2006). By creating small holes in the SCB plate, events analogous to the body's natural response to fracture healing takes place. First, blood and marrow elements flow into the defect and fill it, which is similar to the haematoma phase of fracture healing (Wraighte and Scammell, 2006). Next, MSCs within the marrow elements differentiate, initially forming a reparative granulation superclot (Sgaglione et al., 2002), analogous to the inflammation phase (Wraighte and Scammell, 2006). Finally, the repair phase is initiated and new cartilage and fibrocartilage form. In effect, small fractures to the SCB result in the eventual creation of new cartilage, hence the name microfracture surgery.

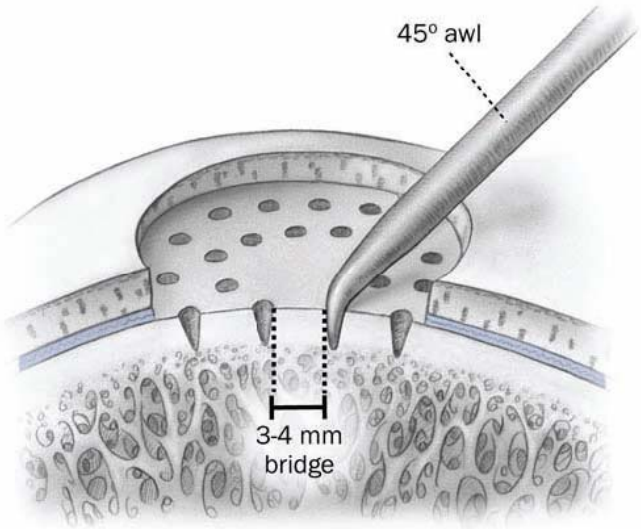

Figure 8: Microfracture surgical procedure
Drawing shows the use of an arthroscopic awl to penetrate SCB and proper spacing of holes during the microfracture procedure. From (Mithoefer et al., 2006).

When the joint in de-pressurized once the arthroscopic pump is turned off blood and marrow flows out of the holes and into the defect (Figure 9).

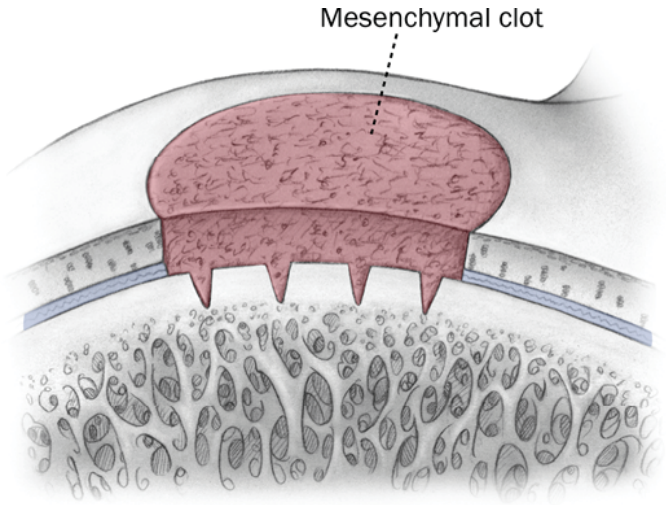

Figure 9: Microfracture post-surgery
Drawing showing defect filled with marrow elements following microfracture surgery. The mesenchymal clot is sometimes referred to a "superclot." From (Mithoefer et al., 2006).

Stored in the marrow are mutipotent mesenchymal stem cells (MSCs) that are able to differentiate into a number of cell types including cartilage cells or chondrocytes. By containing these pluripotent marrow elements, as well as necessary growth factors,

differentiation of MSCs into chondrocytes is possible and ultimately new, healthy cartilage can develop (Lewis et al., 2006).

1.3.5 Autologous Chondrocyte Implantation

The autologous chondrocyte implantation (ACI) procedure (Figure 10) is similar to microfracture surgery in that the ultimate goal is to mechanically influence cells within the defect to generate new, healthy hyaline articular cartilage. However, the two-stage surgical procedure is different than that of the single-stage microfracture surgical procedure. When the defect has been diagnosed, a cartilage biopsy is performed during the first stage, with a sample being taken from a non-weight bearing region of the knee (Lewis et al., 2006). The harvested cartilage is cultured and chondrocytes isolated, which is then followed by a multi-week or multi-month period during which the chondrocytes are allowed to multiply (Riegger-Krugh et al., 2008). The second phase, implantation, begins with lavage and debridement of the defect, with it being very important that the defect is shouldered by a healthy, stable rim of cartilage, as it is in microfracture surgery. A periosteal flap slightly larger than the size of the defect is then obtained and sutured over the defect, which serves a means of containment for the chondrocytes (Figure 11), which are subsequently injected into the defect.

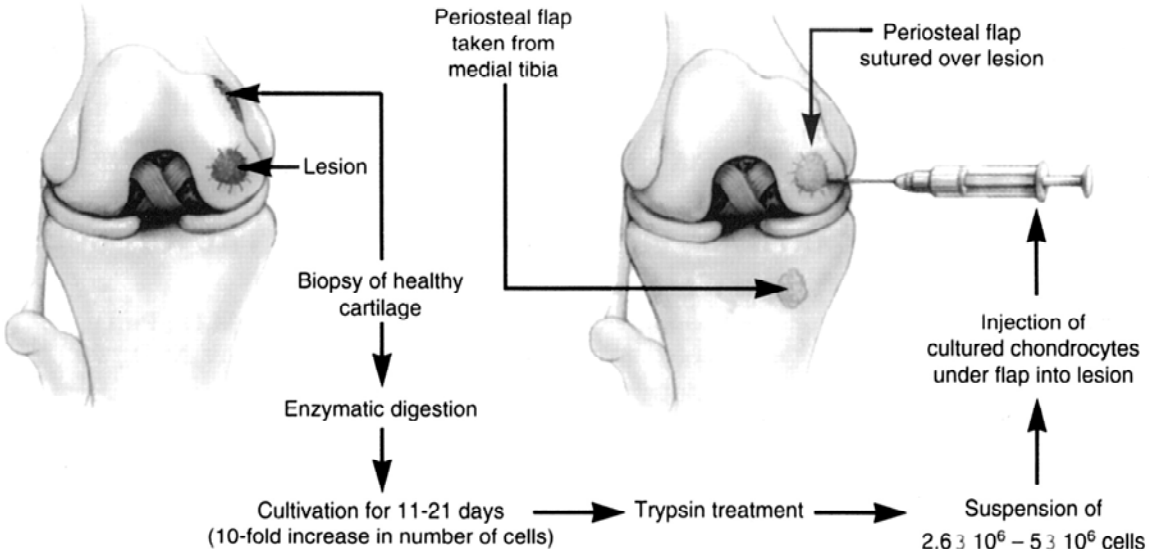

Figure 10: Autologous chondrocyte implantation procedure
This diagram shows explains the sequence of events in ACI, from biopsy procurement, cultivation of cells, periosteal flap procurement and suturing, and injection of cells. From (Mandelbaum et al., 1998).

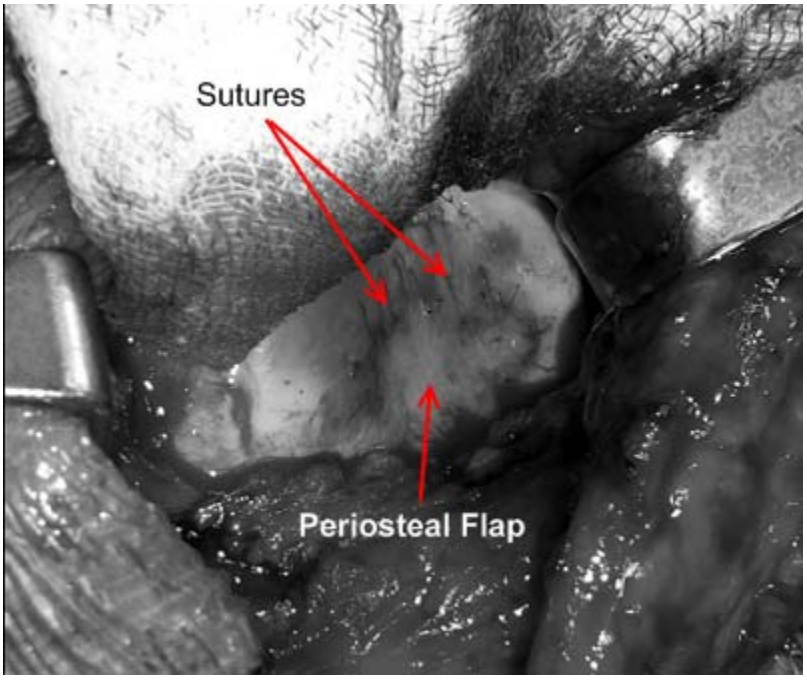

Figure 11: Autologous chondrocyte implantation
Periosteal patch is sewn to neighboring healthy articular. Chondrocytes are then injected into the defect. Adapted from (Lewis et al., 2006).

The ideal result of both microfracture surgery and ACI is the complete filling in of a cartilage defect with repair tissue that has the same mechanical properties and durability as the surrounding hyaline cartilage. It has repeatedly been shown that in vivo the MSCs released into a defect during microfracture surgery are able to differentiate into chondrocytes and eventually into healthy hyaline cartilage. Similarly, chondrocytes harvested from a donor site and cultured with appropriate growth factors and nutrients have been implanted into defects during ACI and successfully resulted in the same hyaline cartilage (Knutsen et al., 2004). For this to happen, a source of mutipotent cells must be contained within the defect and a mechanical stimulus must be applied in order to create the correct differentiation pathway that leads to hyaline cartilage. Concepts described by the theory of mechanobiology have been developed to explain and predict how cells differentiate into various tissue types when subjected to external loads.

1.4 Mechanobiology

In 1892, Julius Wolff, drawing on his experiences as both a surgeon and anatomist, presented a theory that bone transformation, now referred to as bone modeling and remodeling, is dependent on the applied stresses acting on it (Maquet, 1992). This idea come to be known as "Wolff's Law," and, at some point in history, was condensed into the simple statement "form follows function." Around the same time, in 1895 Roux developed the concept that undifferentiated connective tissue, when subjected to compression would become bone and when subjected to tension would become fibrous tissue. Roux also believed that cartilage resulted from tissue being subjected to shear (Maquet, 1992). An extension of Wolff's Law, mechanobiology is the study of the cascade of biological events

that begin with a force applied on tissue and result in the differentiation of cells within the tissue (van der Meulen and Huickes, 2002).

More recently Pauwels (1973), in an attempt to present a more quantitative model of skeletal tissue differentiation, developed concepts that have become the basis for subsequent work in mechanobiology. He realized that in a compressible, elastic, and isotropic material octahedral, shear stress and hydrostatic compressive stress lead to volumetric and distortional strain, respectively. Put simply, when a material is subjected to hydrostatic compressive stress, there is a volumetric change and when it is subjected to a shear stress, there is no volume change but distortional strain occurs. This distortional strain then results in elongation of the material, or tensile strain (Figure 12).

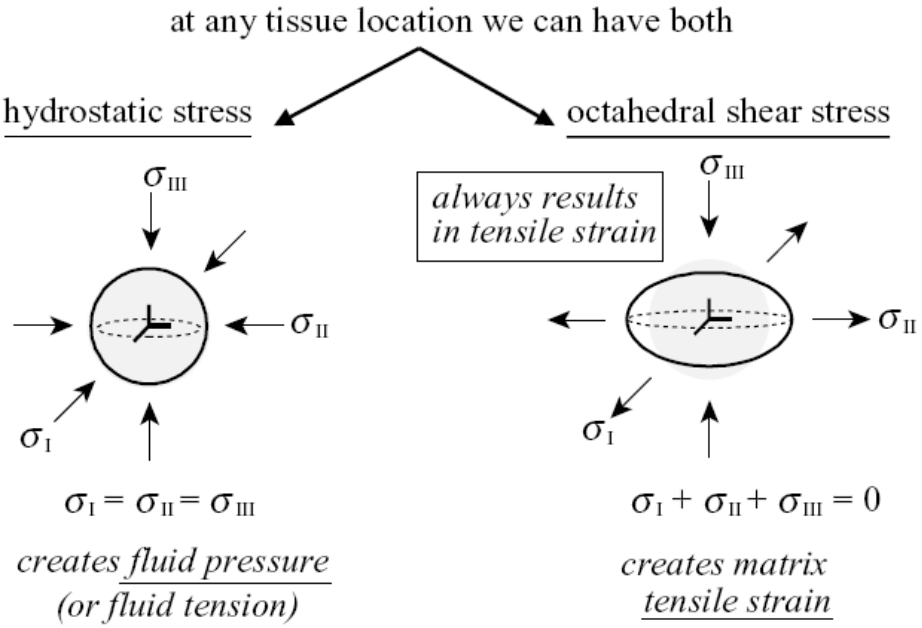

Figure 12: Hydrostatic and octahedral stress
Schematic representation of the deformation caused by hydrostatic stress and octahedral shear stress. From (Carter and Wong, 2003).

Making assumptions about the forces on skeletal tissue in angulated fracture, Pauwels then applied these concepts of mechanics to skeletal tissue. He concluded that hydrostatic

compression was the mechanical stimulus that led to cartilage formation, elongation led to fibrous connective tissue, such as tendons, and a combination of the two stimuli led to fibrocartilage, such as vertebral discs and menisci (Figure 13) (Pauwels, 1973). Pauwels was unsure of the mechanical stimulus that led to the development of bone (Carter et al., 1998).

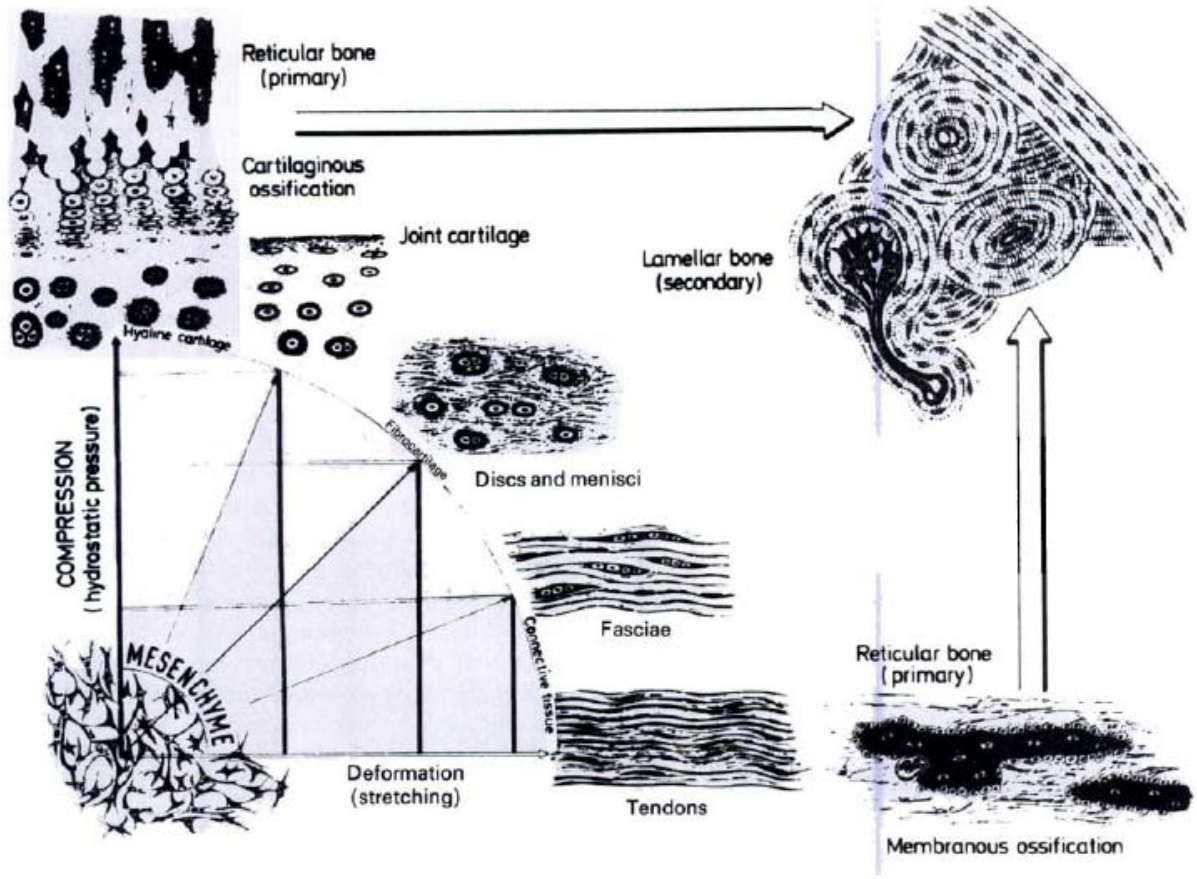

Figure 13: Tissue phase diagram by Pauwels

Pauwels proposed an explanation for the effect of tissue loading history on skeletal tissue regeneration with mesenchyme as the predecessor. Compression (hydrostatic compressive stress) leads to hyaline cartilage, deformation (tensile strain) leads to connective tissue, and a combination of the two leads to fibrocartilage. From (Pauwels, 1973).

Building on the Pauwels' research, Carter et al. (1998) further developed a model for predicting how the mechanical loading history of MSCs determines the generated tissue type. They presented a more comprehensive model and a similar tissue phase diagram (Figure 14), which also proposed a loading history that resulted in bone. In order for bone to form, a

history of low levels of strain, along with low levels of hydrostatic stress is necessary, provided there is adequate vascularity (Loboa et al., 2001). Fibrous tissue results from low levels of hydrostatic stress with significant shear or tensile strain history. Cartilage generation occurs as a result of low tensile strain and significant hydrostatic compressive stress, and fibrocartilage will form in regions of both high tensile strains and high negative hydrostatic stress (Carter et al., 1998; Loboa et al., 2001). From this model the most important hypothesis of mechanobiology was presented, that compressive hydrostatic stress generates or maintains cartilage and shear or tensile strains damage cartilage and lead to ossification, thereby creating bone (Carter and Wong, 2003). When considering the mechanical environment in the knee joint, these concepts are logical, and seem to support the Wolff's fundamental law that form follows function. When tissue is subjected to compressive forces alone, durable and extremely compression-resistant cartilage develops. On the contrary, tissue that is subjected to high levels of tensile strain becomes fibrous tissue that is well suited for stretching and deforming. When the mechanical environment includes a combination of tensile strain and hydrostatic compressive stress, a combination of cartilage and fibrous tissue forms.

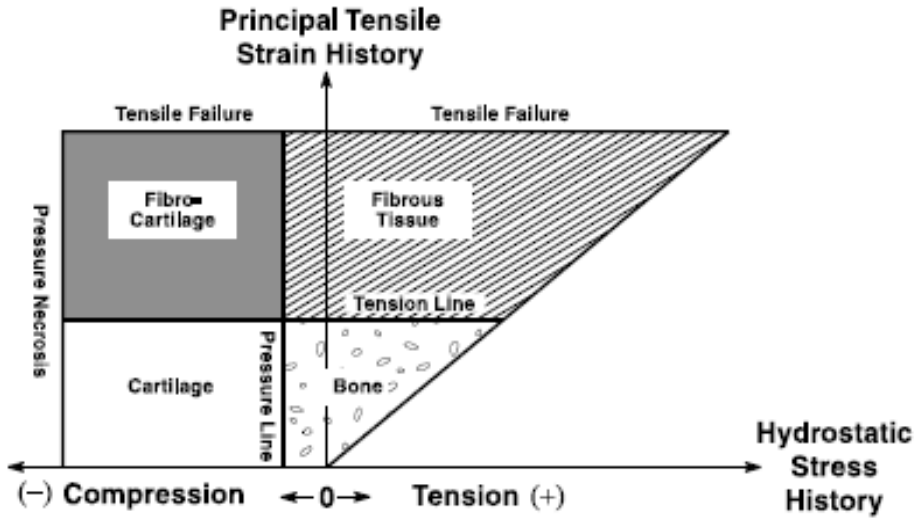

Figure 14: Tissue phase diagram by Carter et al.
Carter et al. built upon the model by Pauwels, further explaining the effect of tissue loading history on skeletal tissue regeneration. From (Carter et al., 1998).

In addition to providing an explanation of tissue differentiation pathways, the phase diagram incorporates the idea that extreme levels of hydrostatic compressive stress, regardless of the level of superimposed tensile strain, will result in pressure necrosis (Loboa et al., 2001). Extreme compression of the cartilage leads to chondrocyte death, in a similar manner as blunt impacts to cartilage.

1.5 Application of Mechanobiology to Surgical Cartilage Restoration

Mechanobiological theories describe the influence of mechanical stresses and strains on the differentiation of MSCs into one of four tissue types. Surgical cartilage restoration techniques, namely microfracture surgery and ACI, attempt to utilize the ability of MSCs and chondrocytes, respectively, to differentiate into articular cartilage where a defect has occurred. It is evident therefore, that knowledge of the mechanical forces acting on undifferentiated cells in the defect is crucial for the success of surgical cartilage restorative procedures, such as microfracture and ACI. It should be noted that it is assumed that the

1.6 Osteoarthritis Progression

The degeneration of articular cartilage and its progression to osteoarthritis has been a subject of great interest over a number of decades, and efforts to determine the causes of articular cartilage defects are still ongoing.

A significant amount of research has been conducted focusing on articular cartilage degradation and regeneration in and around defects, both experimentally and computationally. Guettler et al. (2004) developed an experimental biomechanical model using cadaveric knees and demonstrated a rim stress concentration effect for defects 10 mm and greater. They predicted that large deformations of articular cartilage as a result of stress concentrations would cause large shear stress, which could be detrimental to chondrocyte viability. In this study, the authors created circular defects of various sizes on the lateral and

medial femoral condyles, and removed both the cartilage as well as a significant portion of the SCB using a coring device. Bone was removed in order to ensure no contact with the defect, since they were investigating cartilage rim stress.

Brown et al., (1991) showed moderate circumferential stress concentrations at the rims of defects when compared with contact stress recorded at the surface of intact cartilage in dog knees. They found an elevated contact stress gradient in the radial direction near defect rims compared with intact articular cartilage and found that contact stress distributions became more non-uniform around the rim as defect diameter was concentrically enlarge from 1 to 7 mm.

Using a biphasic poroelastic finite element model of an osteochondral defect, Kelly et al. (2005) investigated the mechanical stimuli acting on MSCs within a defect during repeated axial ramp loading to 800 N over 0.5 seconds. They analyzed the effect of the calculated mechanical stimuli on the dispersal, proliferation, differentiation, and death of MSCs using a mechano-regulation algorithm based on the mechanobiology tissue phase diagram presented earlier. Among other findings, their model predicted greater amounts of fibrous tissue formation as the size of the defect is increased and large strains were predicted within the fibrous tissue, resulting in significant cell death.

Using an in vivo model with canines, Nelson et al. (1998), showed the mechanically inferiority of fibrocartilage in a 6-mm defect, as it was incapable of reducing contact rim stress.

Though both experimental and computational results, Shapiro et al. (1993) showed bone formation through in the base of the defect, cartilage formation in the center of the defect, and fibrous tissue formation superficially. They suggested that the high strain and

fluid flow at the articular surface generates fibrous tissue formation and inhibits chondrogenesis, causing OA progression.

Pena et al. (2007) created a 3-dimensional finite element model based on MRI data to investigate the effect of size and location of osteochondral defects in arthritis. They found that in larger defects the contact stress around the rim strongly increased, contrary to the case of smaller defects (<1 cm^2). Furthermore, they predicted increased compressive stress in large defects indicated a mechanical overloading effect that would lead to continued degeneration.

1.7 Objectives

Cartilage defect morphology is an important factor in both progressive chondral degeneration as well as prescription of an appropriate clinical reparative procedure. Clinical algorithms for chondral defect management generally use 2 cm^2 as a size threshold, beyond which damage to adjacent cartilage or subchondral bone become likely. However, there is little biomechanical data or clinical evidence to support this size. Furthermore, clinical models are arbitrarily based on diameter or area of strictly circular defects and do not consider defect shape. Experimental biomechanical and computational models have investigated stress concentrations at defect rims and often conclude, based on their findings, that defect size should be considered when prescribing clinical procedures.

There are no known experimental studies that investigate the existence of a defect size threshold or critical diameter at which the femoral SCB contacts the opposing cartilage of the tibial plateau. Furthermore, to the knowledge of the author, there are no studies which consider the shape or orientation of a defect and the subsequent effect of these defect features

on SCB contact.

Therefore, through experimental biomechanical testing, the objective of this research is to investigate the effect of cartilage defect size and morphology on the presence of contact between the SCB within a defect and the opposing cartilage surface, with the assumption that increased SCB contact is deleterious to the restoration process.

This thesis contains six chapters. Chapter 2 will discuss the design and fabrication of a test jig for loading of knee specimens. Chapter 3 presents the methods used to accomplish the study's goal, including the experimental setup and protocol. Chapter 4 presents the results an analysis from the experimental testing. Chapter 5 is a discussion and conclusion will be presented in Chapter 6. A bibliography and an appendix are included at the end.

Chapter 2: Design and Fabrication of Test Jigs

2.1 Design and Fabrication of Test Jigs

The initial phase of the project was to design two identical test jigs for securing knee specimens to facilitate the quasi-static joint loading. One was to be installed on the base of the text fixture and the other on the movable upper portion. The jigs were to be designed for use in studies other than just the present one, and so an amount of operating flexibility was desired. Some of the requirements were that the jigs be compatible with multiple loading frames, be capable of simulating a range of knee flexion angles from 0° to 90°, be able to secure both human as well as bovine knee specimens. An initial concept jig (Figure 15) was designed that was comprised of two separate parts: the MTS Jig, which was bolted to the MTS test frame, and the Specimen Jig, which was to rotate relative to the MTS Jig with the test specimen secured.

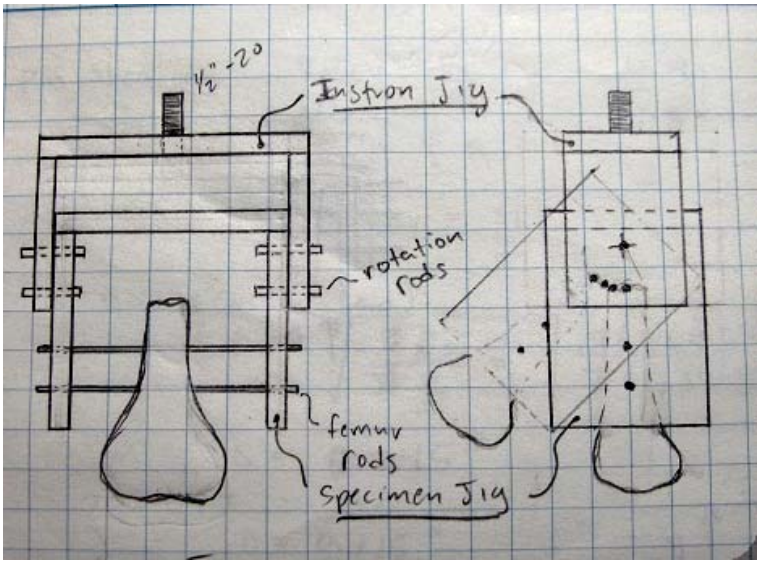

Figure 15: Initial jig sketch

The initial jig design was comprised of two jigs, a rotating part, labeled Instron (MTS) Jig, and a stationary part, labeled Specimen Jig.

The plates that make up the sides and top sections of the jig were fabricated from aluminum because of its combination of strength, weight, and ease of manufacturing. A stress analysis was performed to determine the necessary plate thickness to prevent failure. Several failure modes were assessed, including bending failure of the upper plate from the applied axial force, edge shear out from the rods, and edge tearing from the rods, all assuming a conservative value of 11 ksi for the tensile yield stress of aluminum. Bending of the side plates was also examined, using the worst-case situation for bending, which is when both fixtures are placed at 45° flexion. With a plate thickness of 0.5", the maximum applied force was prior to yielding was calculated to be over 9000 N. The initial concept was altered after it was determined that the Specimen Jig width could be significantly decreased from 4" to 2.25" and bending stresses would still be well below the yield stress.

Calculations were also performed to determine the material to be used for the rods. Steel was chosen because of its stiffness and strength, as minimal bending was desired during loading. Bending stress calculations determined that minimal bending would occur in a

0.25” diameter rod and that the stress was significantly lower than the conservative assumed yield stress of 100 ksi. The maximum applied force before bending failure was determined to be over 1900 N. It was also determined that the first point of failure would be the yielding of the steel rods due to bending stress, which would be the desired point of failure, as they are replaceable.

Next, the hole pattern on the side plates of the MTS Jig was designed to enable rotation of the knee specimens during flexion simulations. Because two identical jigs were being built, and a maximum flexion angle of 90° was desired, the jigs were designed to accommodate flexion angles of 45° each, so that in combination 90° would be possible. The jigs were then modeled using Solid Edge (Figure 16). The lower rotating rod was eliminated, instead choosing to use the upper specimen rod as one of the rotating rods to simplify the design.

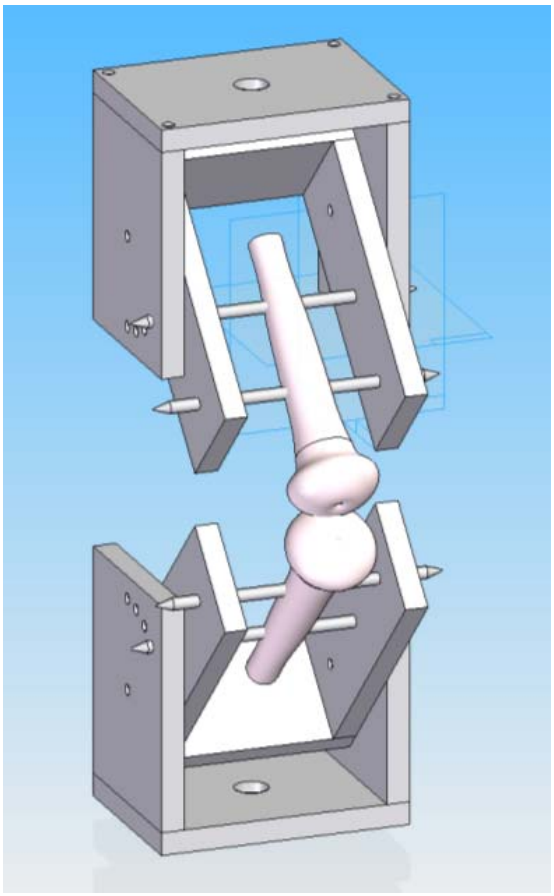

Figure 16: Solid Edge model of custom jigs

This computerized image of the custom jigs shows a knee joint at 90° flexion. Though testing was completed at full extension, the jigs will be used in future studies investigating joint biomechanics at various flexion angles.

Following the design of the jigs, aluminum plate stock was purchased from Research Alloys Co., Inc. and machining was performed in the OSU Mechanical Engineering Student Machine Shop. The jigs were then assembled and installed on the MTS test frame (Figure 17) prior to testing for evaluation purposes.

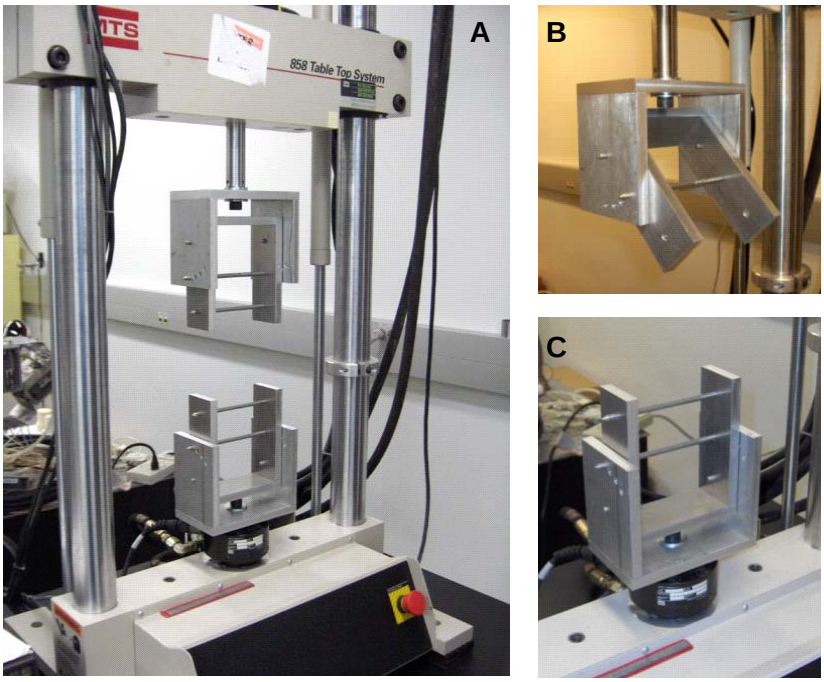

Figure 17: Custom jigs installed on test frame
(A) Completed jigs installed on the test frame, at the 0° flexion (full extension) position, (B) Femoral jig at the 45° flexion position, (C) Tibial jig at the 0° flexion (full extension) position

Chapter 3: Experimental Methods

3.1.1 Experimental Specimen Groups

Twelve fresh-frozen bovine knees were obtained from two local slaughterhouses for use in testing. They consisted of five right knees and seven left knees. Age and sex of the subjects were unknown. Each knee specimen included the distal 4"-6" of the femur and the proximal 4"-6" of the tibia. The presence of lesions, fibrillation, fissures, or cartilage softening excluded knees from the study. The knees were randomly separated into three test groups, based on the defect shape to be created. Group I consisted of specimens with circular defects (Figure 18a). Group II consisted of specimens with oval defects with the long axis in the coronal plane (Figure 18b). Group III consisted of specimens with oval defects with the long axis in the sagittal plane (Figure 18c).

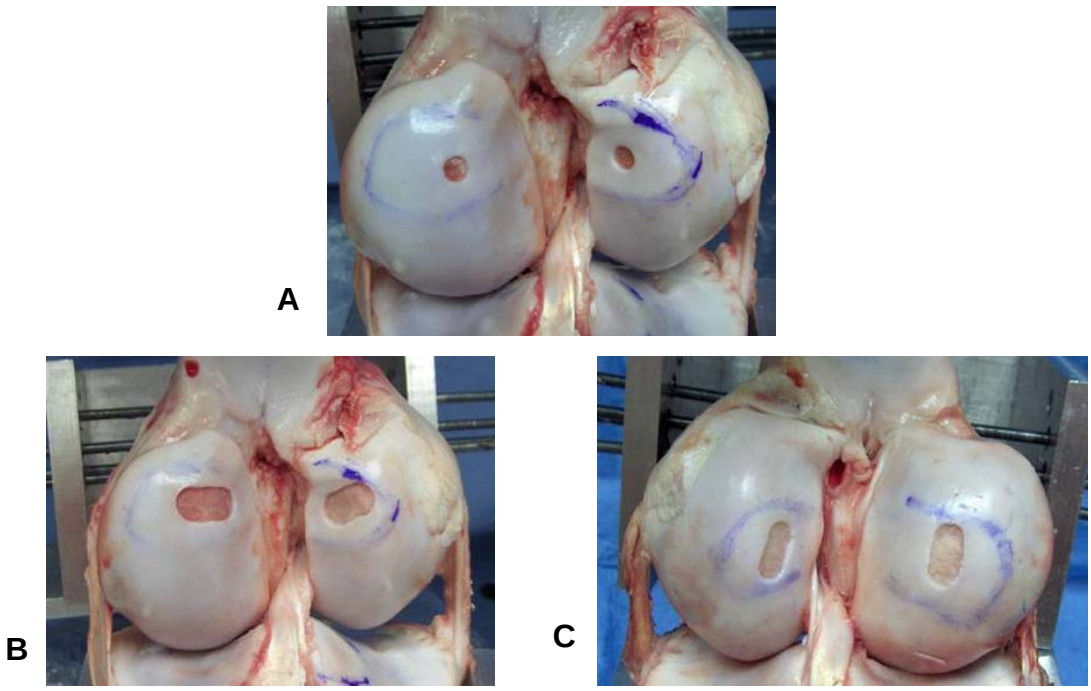

Figure 18: Photos of specimens from the three defect groups
(A) Circular defects; (B) Oval defects with long axis in coronal plane; (C) Oval defects with long axis in sagittal plane

3.1.2 Determination of Appropriate Load

In the literature there are a number of established loading protocols for biomechanical testing of articular cartilage defects. Because of the viscoelasticity of articular cartilage, its deformation is dependant not only on an applied load, but also on the rate of applied load. In the majority of quasi-static experimental studies simulating joint loading, the joint is subjected to a ramp load and then the maximum load is held for a period of time, followed by a negative ramp load back to zero. Guettler et al. (2004) used a ramp load to 700 N, which was then held for 5 seconds. They found that the maximum recorded contact stress occurred during the constant load of 700 N. Kelly et al. (2005) used an axial ramp load of 800 N in finite element model investigating tissue spontaneous tissue regeneration. Pena et al. (2005) used a vertical axial load of 1,150 N, citing this value as the approximate force on the knee

during a normal gait cycle at full extension.

The common maximum load of 700 N - 1,150 N is approximately equal to the body weight of a full size adult male and, as stated above, is the approximate force during a normal gait cycle. However, because the referenced studies used human knees, these values may not be appropriate and the present study using bovine knees. These studies were concerned with joint loading during a normal gait cycle. However, this study focuses on the mechanical forces in a defect following a surgical cartilage restorative surgery such as microfracture surgery or ACI. It has been shown that post surgery rehabilitation is most effective when weight bearing is minimal immediately following surgery and that the healing tissue should be protected from significant loads for six to eight weeks (Steadman et al., 2001; Riegger-Krugh et al., 2007). It would be undesirable to attempt to simulate loading during a normal gait cycle since it would be against recommended post-surgery rehabilitation programs to subject the knee to such high loads. To simulate minimal weight bearing of a 6,000 N cow, a load of 1,000 N was chosen.

3.1.3 Mechanical Testing System

Experimental biomechanical loading was performed on bovine knee specimens using an MTS Bionix 858 axial-torsion servo-hydraulic materials test system. The system was equipped with a dedicated microcomputer and TestStar software for instrument control. The system is capable of open loop and closed loop feedback control of actuator axial load and displacement, as well as actuator torsion and rotation. Only axial load control was used for this study. The custom jigs were installed on the test frame with the tibial jig fixed at the base and the femoral jig mounted to a load cell in line with the hydraulic actuator, for which rotation was not constrained.

3.1.4 Tekscan Contact Pressure Measurement System

Contact pressure and area measurements were obtained with digital electronic pressure sensors (K-scan 4000, Tekscan, Boston, MA), which provide a reliable and accurate method of measuring joint contact pressure and area (Drewniak et al., 2007; Harris et al., 1999). Two sensors designed for the medial and lateral joint compartments each contain a sensing area of 28 mm x 33 mm, made up of 572 individual sensels of 1.6129 mm^2. The sensors utilize a matrix of perpendicularly oriented lines of piezo-resistive ink which conduct current, thereby sensing contact (Figure 19).

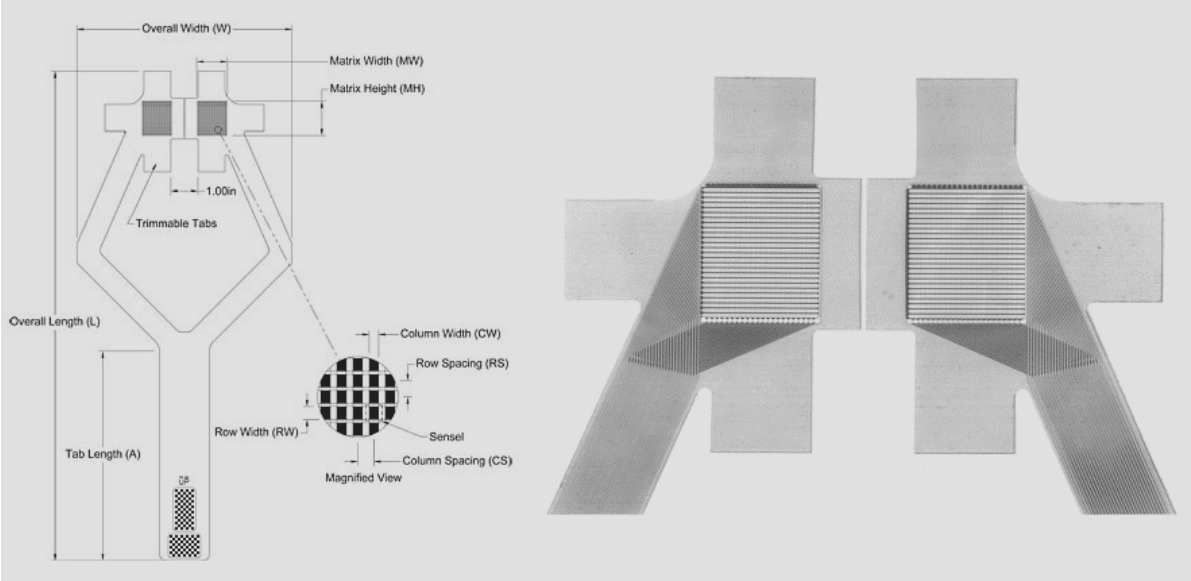

Figure 19: Tekscan K-Scan 4000 contact pressure sensor
Diagram on left shows a schematic of the contact pressure sensor used in the study (From Tekscan). Note the magnified view demonstrating the matrix of perpendicularly oriented piezo-resistive lines. The photo on the right shows a magnified view of the sensors (from Harris et al., 1999).

The sensors interface with a handheld data acquisition device, which is then connected to the USB port of a laptop computer (Dell Latitude D820, Dell Inc., Round Rock, Texas). A software program loaded on the laptop computer (I-Scan Pressure Measurement System, Tekscan, Boston, MA) performs calculations to generate plots of contact area. Calibration of

the software to a known applied force allows the system to calculate contact pressure measurements.

3.2 Testing Protocol

3.2.1 Specimen Preparation and Setup

All knees were received fresh, and were immediately frozen until use. Knees were thawed at room temperature for 8-12 hours before testing. Tibial and femoral articular cartilage was examined by eye and with manual probing to ensure cartilage was not arthritic or irregular. Prior to testing, the bovine knee specimens were dissected. The knees were obtained with skin removed. Dissection of the knees first involved removal of subcutaneous adipose tissue, muscle tissue, and connective tissue surrounding the joint using a scalpel. A medial and lateral parapatellar arthrotomy was made and the extensor mechanism was removed to provide access to the joint. The anterior tibialis and popliteus were removed. Because the menisci in a bovine knee cover the majority both the medial and lateral tibial condyles both menisci were removed at their anterior and posterior horn insertions. The cruciate and collateral ligaments were left intact to provide normal joint stability. All remaining soft tissue was dissected free from the distal femur and proximal tibia. Following dissection and prior to executing each test, knee specimens were sprayed with warm water to prevent desiccation.

With the use of hardened stainless steel 5 mm diameter drill bits, the femur was first secured in the upper jig. Four drill bits, providing eight points of fixation, were placed parallel to the joint line. With the femur rigidly fixed, the tibia was secured in the same way, again providing eight points of fixation with the use of four drill bits placed parallel to the

joint line. The knee was positioned such that it was in full extension (Figure 20).

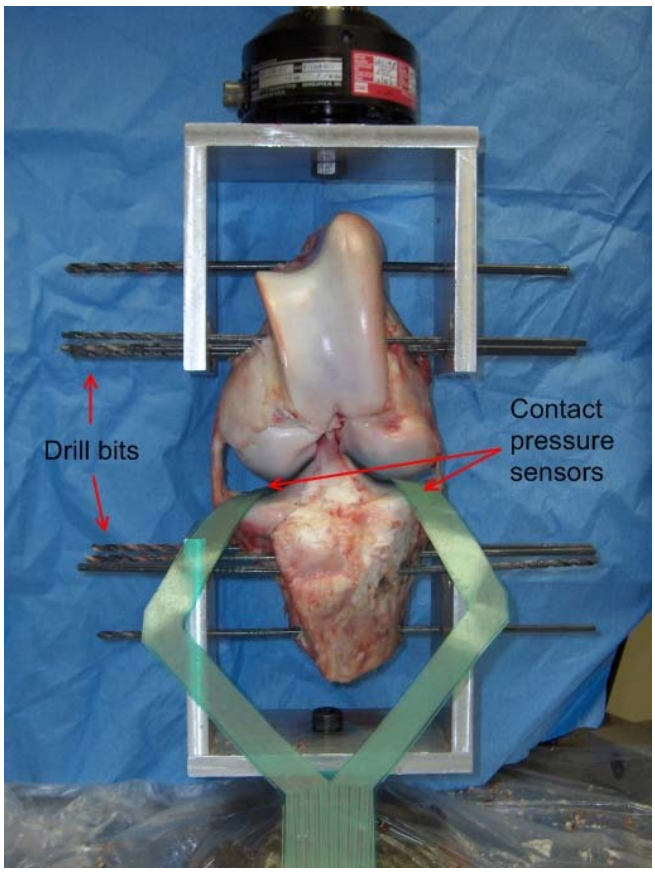

Figure 20: Knee specimen installed in test jigs
Arrows indicate drill bits used to secure knee specimen and Tekscan contact pressure sensors placed in tibio-femoral joint.

To ensure equal distribution of the applied load between the medial and lateral compartments, Tekscan sensors were placed in the joint and a minimal load was applied, so that the opposing cartilage surfaces initiated contact, which could be viewed on the laptop. Adjustments were made until this minimal load produced simultaneous contact in the medial and lateral compartments. This was done to prevent any eccentric valgus or varus loading conditions. At the point where simultaneous contact was initiated, the actuator load cell and displacement potentiometer were zeroed.

Prior to testing, the sensors were conditioned according to the manufacturer's guideline, by applying a ramp load to 1,000 N and then 20 cycles of haversine oscillatory

loading from 700 N to 1,300 N over 40 seconds (0.5 Hz). The sensors were then calibrated using a two-point calibration at 0 N and 1,300 N.

3.2.2 Defect Creation

For each specimen, the following test protocol was employed once alignment and calibration were completed. The Tekscan pressure sensors were placed in the joint space and aligned visually to ensure SCB contact would be recorded. The previously discussed zeroing method using initial contact was performed. A preliminary 1,000 N load was applied and the tibiofemoral contact areas were mapped on the femur using a surgical marker. The mapped area was bisected in the sagittal and coronal plane to locate the correct placement of the intended chondral defects. The load was then removed and the actuator returned to the zero position. The upper jig was unlocked from the load cell and the joint flexed to expose the femoral articular cartilage. A circular hollow punch was then used to create the initial defect, which was centered at the intersection of the bisection lines. Debridement was performed using an arthroscopic curette.

Creation of the oval defects utilized an additional step. The defect was created with the same cylindrical coring device, but two tangentially connected defects were first created and then an incision was made to create the defect edge parallel to the long axis (Figure 21). Debridement of the defect was then performed using an arthroscopic curette. The defect was thus characterized by a long axis, 2d, that was equal in length to twice the short axis, d (Figure 21).

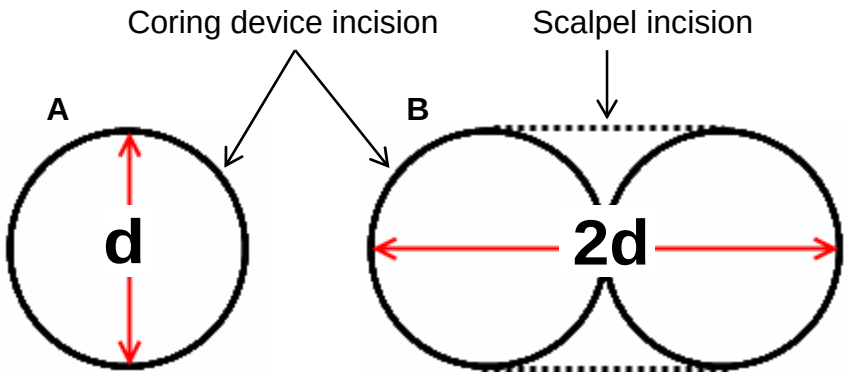

Figure 21: Schematic of defect creation method and sizing
(A) Circular defects were created using a cylindrical coring device to make the edge incision; (B) Oval defects were created with the same cylindrical coring device (solid lines), followed by a scalpel incision to created the long edge of the defect (dotted lines). Sizing of defects is shown as well. Circular defect diameter, d, is equal to the oval defect short axis.

The importance of debridement should not be overlooked, as it plays a key role in SCB contact. Removal of all layers of the articular cartilage, including the calcified layer, is crucial to exposing SCB (Figure 22). Special care was taken to ensure that this was performed when each defect was created. The specimen was sprayed with warm water and the jig was then re-fastened to the load cell.

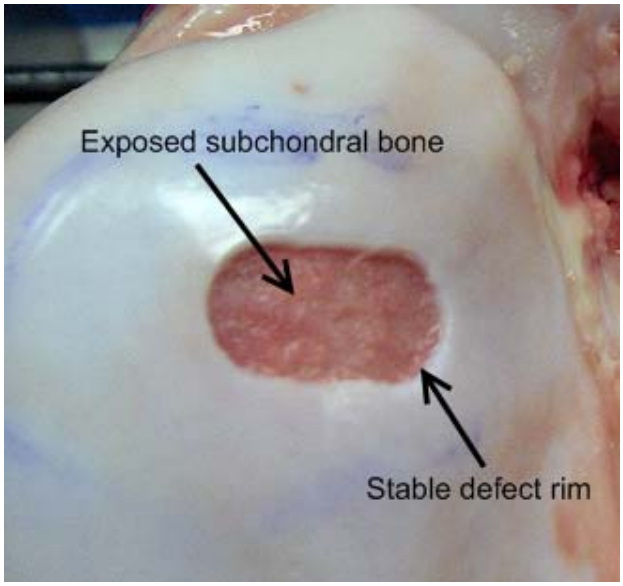

Figure 22: Zoomed image of oval defect
Arrows point to the exposed SCB and the stable rim of a simulated oval defect. Both features are important for a successful surgery and were reproduced for this study.

The sensors were re-inserted into the joint space, taking care to avoid bending or crinkling. The knee was loaded at a rate of 20 N/s to 1,000 N, which was held for 10 seconds and contact measurements were recorded using the I-Scan software system. The knee was then unloaded at a rate of 50 N/s. The fixture was then unlocked from the load cell the defect was concentrically enlarged, and again loaded using the same ramp loading procedure. During loading, real-time contact pressure measurements were displayed graphically on a connected laptop computer with the previously mentioned software system. This procedure was repeated with progressively larger defects until SCB contact was visualized on the laptop computer. Defects ranged from 5 mm in diameter to 25 mm in diameter, which correlate to clinically relevant defect areas of 0.2 cm^2 to 5.7 cm^2. This procedure was performed four times for each of the three defect shapes, using a total of 12 knees.

Following testing, the medial and lateral condylar with and depth of each knee were measured manually and recorded. The depth of each defect was measured using a digital caliper. The depth measurement was performed at a later date to avoid the effects of any residual tissue compression from loading.

3.3 Data Analysis

3.3.1 MATLAB Contact Area Measurements

In order to determine the degree of SCB contact for each loading test, a measure of SCB contact area was necessary. The I-Scan Contact Pressure Measurement System is designed to determine the contact pressure between two surfaces. Because the calculation of contact pressure is determined from a sensed area, calibrated to a known force, the sensors are ideal for determining contact area. However, there are some limitations to the software,

namely when the desired area measurement is for a partial section of the sensor. The I-Scan software includes a function to calculate the area inside a user-defined region, but this region is limited to rectangular shapes. The region of concern for this project was a circular region of SCB and thus the built-in capabilities of the software program were inadequate.

A custom MATLAB program was written to calculate SCB contact area. The program uses the contact pressure output of the thin film sensors (Tekscan) as its input, as well as the nominal diameter of the created defect. Contact was considered to have occurred at a sensel if a nonzero contact pressure value was registered at that point. In addition, if there was a nonzero pressure value at a sensel, then it was assumed that contact occurred at the entire area represented by the sensel.

Because the defect location on the sensor was variable from test to test, it was necessary to provide the capability to identify the center of the defect in the matrix of sensel locations. An interactive program was created in MATLAB, such that it was possible to visually indicate the assumed defect center and then calculate the contact area that occurred within the defect. First, the program prompts the user to indicate the file name and defect radius. A contour plot is generated using the MATLAB "contourf" function, which creates a plot of contact pressure. The plot's x-axis represents the location along the short dimension of the Tekscan sensor and the y-axis represents the location along the long dimension of the Tekscan sensor. Next, the program instructs the user to identify the center of the defect. This was accomplished using the MATLAB "ginput" function. Crosshairs appear on the cursor and, when the mouse is clicked on the contour plot, the x and y coordinates are saved. The program then calls these coordinates and uses the parametric equation of a circle to overlay a circle of the indicated diameter at the chosen location.

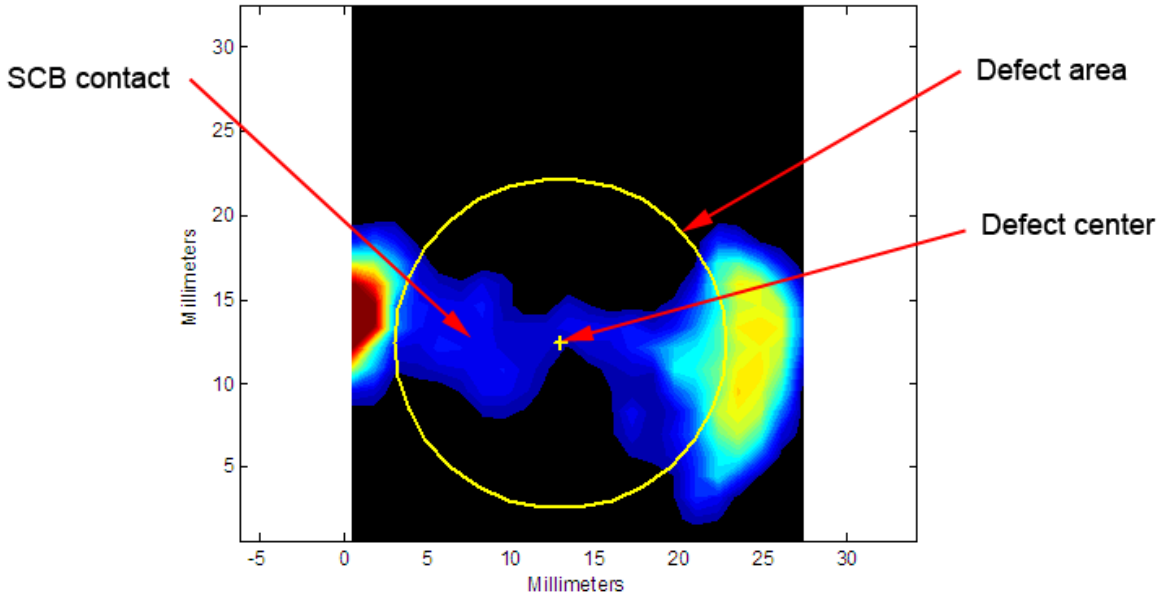

Figure 23: Interactive MATLAB contact area measurement plot
The contour plot represents the contact pressure at each sensel location, with the magnitude represented by the color. The yellow cross and circle are the defect center and outline, respectively, identified by the user using interactive plotting features in MATLAB. SCB contact area was calculated from the accompanying MATLAB program.

After receiving confirmation that the circle is in the correct position, the program determines the number of sensels that have a nonzero pressure value within the indicated circle. With a known sensel area of 1.6129 mm^2, the total area being contacted is simply the number of sensels registering a nonzero contact pressure multiplied by the area of a single sensel. This procedure was completed for each contact pressure file recorded during testing and tabulated for data analysis.

3.4 Statistical Analysis

Statistical analysis of SCB contact area measurements was performed using SPSS 16.0 for Windows (SPSS Inc., Chicago). Initially, a one-way analysis of variance (ANOVA) was performed to determine the statistical significance of differences in the mean SCB contact area measurements of each defect size. This was performed for each of the three

defect shape groups. For the analysis the factor was the defect size (diameter for Group I, short-axis dimension for Groups II and III), with the different defect sizes as factor levels. Because repeated pair-wise comparisons using the specified significance level are not appropriate, whenever the one-way ANOVA indicated significant differences, a post-hoc test was performed using the Dunnett's T3 test for multiple comparisons of group means with unequal sample sizes and unequal variances. This post-hoc test was chosen because the results were found to have unequal variance and unequal sample sizes. T-tests and paired T-tests were also performed, not assuming equal variances. For all analyses, a level of statistical significance of $\alpha = 0.05$ was assumed. Mean values are reported ± standard deviation.

Chapter 4: Results

Contact pressure measurements from bovine knee joints were obtained using thin film pressure sensors (Tekscan) and the corresponding SCB contact area measurements were calculated for three groups based on the chondral defect location. Group I consisted of knees with circular defects and Group II, medial-lateral ovals (ML), consisted of knees with oval defects with the long axis in the medial to lateral direction, and Group III, anterior-posterior ovals (AP), consisted of knees with oval defects with the long axis in the anterior to posterior direction.

4.1 Group I - Circular Defects

The one-way ANOVA of circular defects demonstrated that there were significant differences among the SCB contact area means ($p=0.00$), without distinguishing between medial and lateral defects. The mean SCB contact areas for the all defects are presented in

tabular form (Table 1) and graphical form (Figure 24). The analysis exhibited a trend of statistically significant increasing SCB contact areas as defect size increased.

Table 1: Descriptive Statistics for Circular Defects

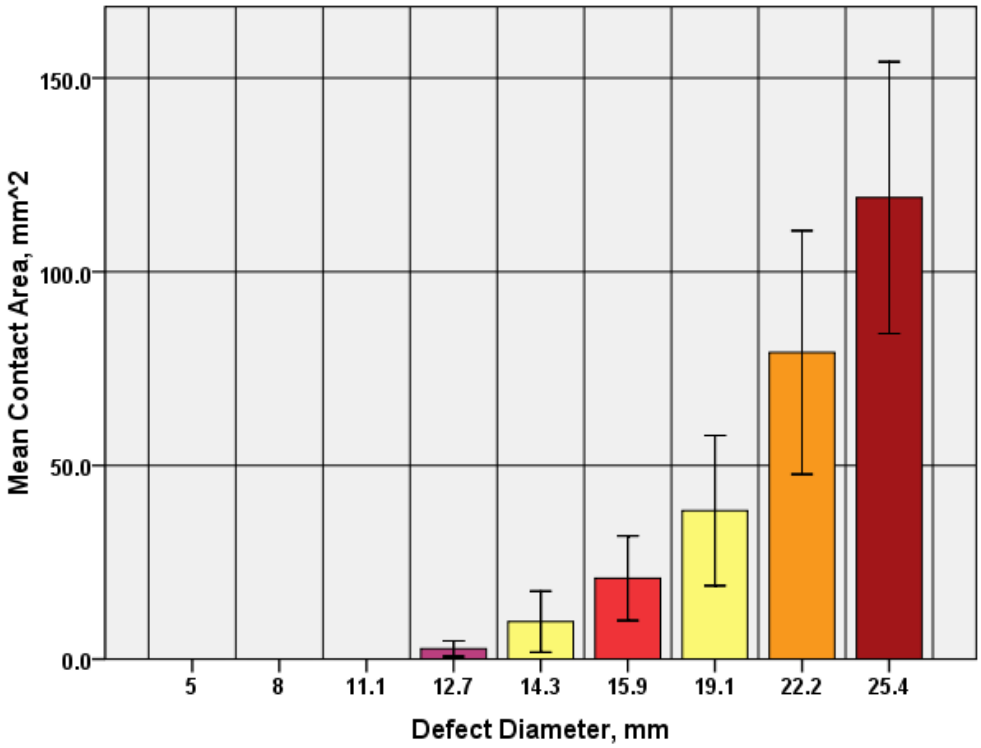

Figure 24: Bar Graph of Circular Defect SCB Contact Area means
Graph shows the general increasing trend in SCB contact pressure as the diameter of circular defects was increased. The 95% confidence intervals are depicted as well.

4.1.1 Mean SCB Contact Area

In defects below 12.7 mm, no SCB contact was demonstrated, and thus the mean of the 5 mm, 8 mm, and 11 mm defects was exactly 0 mm^2 and there was no significant difference among those defect diameters (p=1). The mean SCB contact areas of the 12.7 mm and 14.3 mm defects were found to be 2.7 ± 3.2 mm^2 and 9.7 ± 9.4 mm^2, respectively. The mean SCB contact area of both of these defect sizes was found to not be significantly different (p=0.268 and p=0.326, respectively) from those of the defects which all had no contact. As a result, it is logical to conceptually group these defects together as ones that led to minor SCB contact.

Defects of 15.9 mm had a mean SCB contact area of 20.9 ± 17.2 mm^2 and were found to be significantly different from defects with no contact (p=0.038), but not different from defects of 12.7 mm.

The mean SCB contact area for the 19.1 mm defects was 38.4 ± 30.5 mm^2, which was significantly different from defects with zero contact (p=0.030) and significantly different from defects of 12.7 mm (p=0.048). There was no significant difference between the mean SCB contact area of 19.1 mm defects and both the 14.3 mm and 15.9 mm defects (p=0.200 and p=0.912, respectively). Similarly, no significant difference was demonstrated from the mean of the 22.2 mm group (p=0.139). Compared with the 25.4 mm defects, the 19.1 mm defects lead to a SCB contact area that was 103% lower, which was significant (p=0.011).

The mean value for the 22.2 mm defects was 79.2 ± 49.5 mm^2. The comparison tests revealed statistically significant differences between the SCB contact area mean of the 22.2 mm defects compared with all other defect means ($p<0.05$), excluding the 15.9 mm, 19.1 mm, and 25.4 mm groups. Significant differences existed between SCB contact area means

of the 25.4 mm group when compared with all other defects ($p<0.011$) excluding the 22.2 mm defects ($p=0.857$). The mean SCB contact area for the 25.4 mm defects was 119.1 ± 55.2 mm^2.

4.1.2 Medial vs. Lateral Defects

A paired t-test was performed comparing circular defects occurring on the medial and lateral femoral condyles and revealed that the SCB contact in the lateral compartment was significantly higher than that of the medial compartment ($p=0.013$). The SCB contact area in lateral defects resulted in a 50% increase compared with that of medial defects (Table 3).

Table 2: Paired T-Test Results, Medial vs. Lateral Circular Defects

	Mean	N	Std. Deviation	Std. Error Mean
Medial CD Contact Area, mm^2	23.04	52	35.291	4.894
Lateral CD Contact Area, mm^2	38.49	52	58.705	8.141

In addition to increased contact area in lateral defects compared to medial defects, the transition from minor to major contact appeared to occur at different defect sizes for medial and lateral defects (Figure 25). P-values provided refer to the significance of paired t-tests comparing medial or lateral successive defect sizes. The mean SCB contact area for 22.2 mm lateral defects was 85% higher than for 19.1 mm defects (p=0.026), whereas defects on the medial condyle led to an increase of only 39% (p=0.089). When defects were increased from 22.2 mm to 25.4 mm, the mean increase on lateral condyles was 26% (p=0.091), compared to 65% on medial condyles (p=0.078). These results suggest a smaller defect size threshold from minor to major contact in lateral defects compared with medial defects.

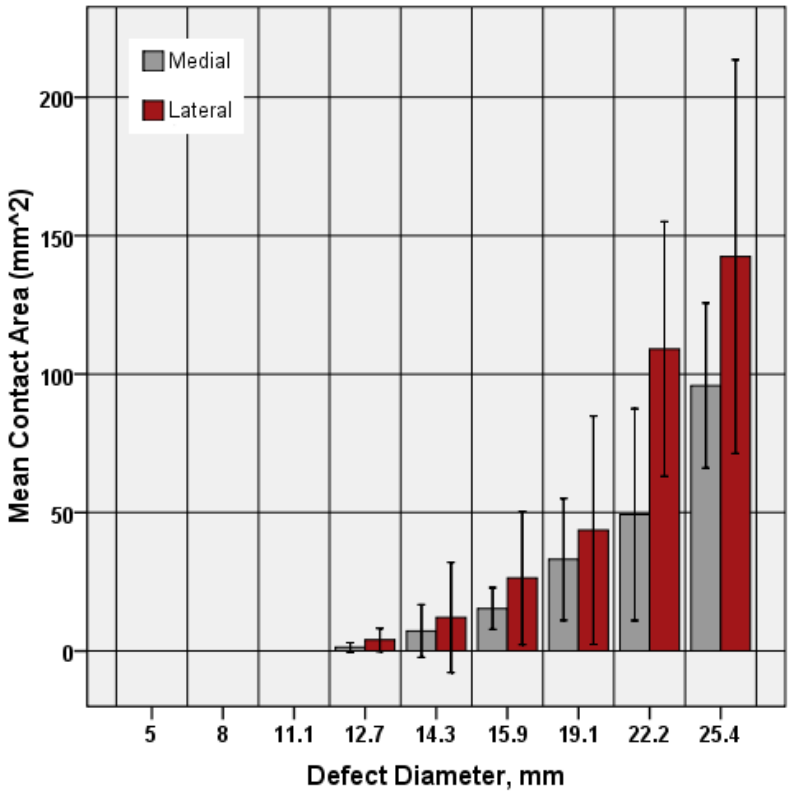

Figure 25: Comparison of Medial vs. Lateral SCB Contact Area
A significant difference was found between the mean SCB contact areas of medial and lateral defects. Lateral defects had 50% higher contact area than medial defects.

4.2 Group II – Anterior to Posterior Oval Defects

Preliminary testing of AP oval defects is presented here.

4.2.1 Mean SCB Contact Area

A one-way ANOVA was performed on the SCB contact area data using Dunnett's T3 method for multiple comparisons. There were no statistically significant differences among the means ($p>0.05$). A comparison of the means is presented (Figure 26). A general trend of increasing SCB contact area can be seen, though no statistical significance was shown. This is likely similar to the trend that occurred in the case of circular defects.

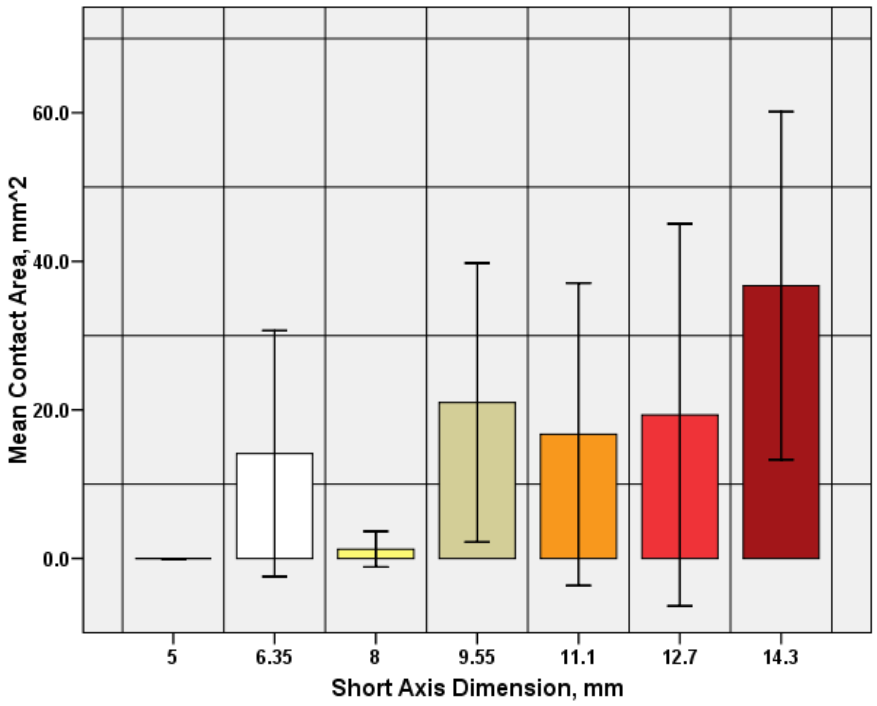

Figure 26: Bar Graph of AP Defect SCB Contact Area means
No statistically significant difference was found between the mean SCB contact areas or AP oval defects. The results presented are from preliminary testing.

A paired T-test comparing the mean SCB contact area of medial and lateral defects was performed and showed a statistically significant difference ($p=0.00$). The lateral defects led to a four-fold increase in mean SCB contact area compared to the medial side.

4.3 Group III – Medial to Lateral (ML) Oval Defects

Preliminary testing of ML oval defects is presented here.

4.3.1 Mean SCB Contact Area

A one-way ANOVA was performed on the SCB contact area data of ML oval defects. There were statistically significant differences among one or more of the means ($p<0.05$) and multiple comparisons were made using Dunnett's T3 method. A comparison of the means is presented (Figure 26). A trend of increasing mean SCB contact area with increased defect size was observed.

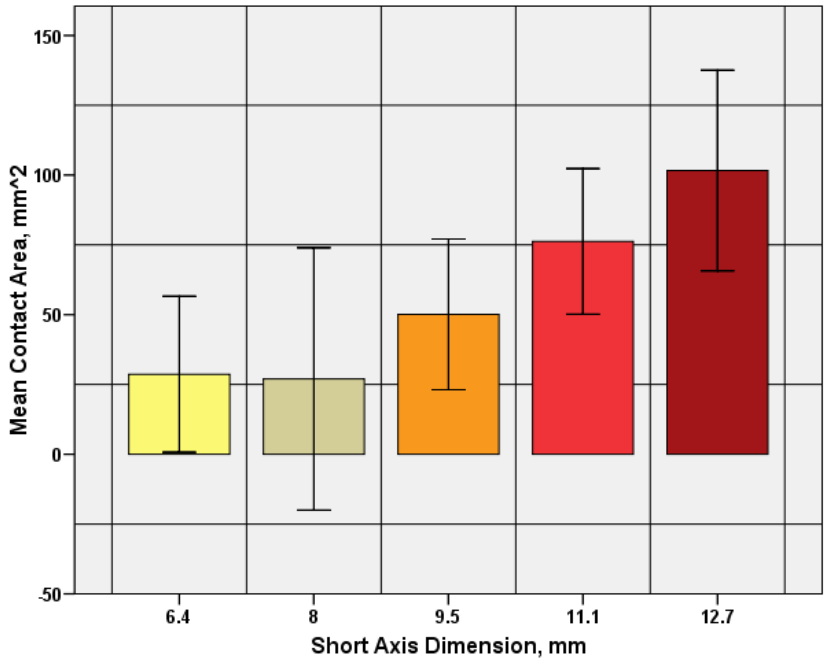

Figure 27: Bar Graph of ML Oval Defect SCB Contact Area means
A statistically significant difference was found between the mean SCB contact areas of ML oval defects of 6.4 mm and 12.7 mm. The results presented are from preliminary testing.

Even with a small sample size, an analysis of multiple comparisons revealed some statistically significant differences in the groups of ML oval defects ($p=0.01$). The multiple comparison test revealed that there was a significant difference in SCB contact means of the

6.35 mm and 12.7 mm defects (p=0.019). No other significant differences were observed. A paired T-test comparing medial and lateral ML oval defects showed a statistically significant difference (p=0.00), with lateral defects resulting in a two-fold increase in SCB contact area compared to medial defects.

4.4 Comparison of Circular and Oval Defects

Due to a small sample size of oval defects tested at this point, the number of tests that could be performed comparing oval and circular defects was minimal, but there were significant results. These are presented here. First, circular defects are compared to ML oval defects, then circular defects are compared to AP oval defects, and finally ML oval and AP oval defects are compared. It is worth noting that throughout testing, oval defects were characterized by the defect short axis dimension. However, some comparisons will be made referring to the defect long axis dimension because by doing this it will be more clear why certain comparisons are being made. Also, all comparisons were performed using T-tests with an adjusted p-value that was calculated not assuming equality of variances and mean values are presented ± standard deviation.

4.4.1 Circular Defects and ML Oval Defects

The SCB contact area means of 11.1 mm circular defects were compared with ML oval defects of the same short axis dimension. It is important to note that the defects of interest here are circular and oval defects with unequal medial to lateral dimensions and equal anterior to posterior dimensions. A significant difference was observed (p=0.00) between the circular defects (0.67 ± 1.3 mm^2) and ML oval defects (75.6 ± 31.1 mm^2).

However, no significant difference (p=0.847) was found in the mean SCB contact

area that resulted from 22.2 mm circular defects (79.2 ± 49.5 mm^2) and ML oval defects (75.6 ± 31.1 mm^2) with 11.1 mm short axis dimensions (22.2 mm long axis dimension in the M-L direction). Similarly, circular defects of 19.1 mm (38.4 ± 30.5 mm^2) were not significantly different (p=0.427) from ML oval defects with 9.55 mm short axis dimension (19.1 mm long axis dimension in the M-L direction) (50.1± 32.3 mm^2).

4.4.2 Circular Defects and AP Oval Defects

Circular defects of 11.1 mm diameter (0.7 ± 1.3 mm^2) were compared with AP oval defects with 11.1 mm short axis dimension, oriented in the M-L direction (27.4 ± 36.4 mm^2). No significant difference was observed (p=0.077). A significant difference was also not observed comparing 12.7 mm circular defects (4.7 ± 4.6 mm^2) with AP oval defects with 12.7 mm short axis dimension, oriented in the M-L direction (19.3 ± 24.5 mm^2).

4.4.3 ML Oval Defects and AP Oval Defects

Comparisons were made between ML oval and AP oval defects with equal short axis dimensions. ML oval (50.1 ± 32.3 mm^2) and AP oval defects (21.0 ± 22.4 mm^2) of 9.55 mm short axis dimension were found to be almost significantly different (p=0.057), but 11.1 mm AP oval (27.4 ± 36.4 mm^2) and ML oval (75.6 ± 31.1 mm^2) defects were found to be significantly different (p=0.013).

Finally, ML oval defects with 6.35 mm short axis dimension (12.7 mm long axis dimensions oriented in the M-L direction) (28.7 ± 26.6 mm^2) were compared with AP oval defects with 12.7 mm short axis dimension (19.3 ± 24.5 mm^2), and no significant difference was found (p=0.542).

Chapter 5: Discussion

5.1 OA Progression Threshold Based on SCB Contact

As was expected, results showed a significant increasing trend in SCB contact area with increasing defect size (Figure 28), and this was true each of the three defect shapes investigated. In the case of circular defects, there was a threshold effect that occurred, when SCB contact significantly increased, and this generally occurred between 19.1 mm and 22.2 mm. Circular defects of this range correspond to defect areas of 2.9 cm^2 and 3.9 cm^2.

A number of clinicians suggest that microfracture is appropriate for defects up to 4 cm^2 (Gill et al., 2006; Mithoefer et al., 2006), while others have found poor outcomes of microfracture surgery in defects larger than 2 cm^2, and prescribe ACI for these larger defects (Jones and Peterson, 2006; Riegger-Krugh et al., 2008). In a study that supported a smaller threshold, Guettler et al. (2004) found a threshold of 10 mm (0.79 cm^2) based on defect rim stress during quasi-static loading of human cadaver knees. They found that the a stress concentration began when defects reached 10 mm in diameter and then did not increase in defects as larger as 20 mm in diameter. It is logical that a threshold based on rim stress would be smaller than that of SCB contact, such as a threshold closer to 20 mm suggested in our findings, since SCB contact would generally occur after the rim has been contacted and compressed considerably. Furthermore, in a recent study by Knutsen et al. (2004), it was found that microfracture performed very well in 40 patients with mean femoral defect sizes of 4.5 cm^2, after two years post-operation. Results of microfracture surgery were statistically better or the same as those of 40 defects (mean 5.1 cm^2) treated with ACI in the same study, based on the authors' scoring methods. This result may support a progression threshold

closer to 4 cm^2, as the findings of our study suggest, rather than the $2cm^2$ that is most widely used today.

The results of this research may shed light on this discrepancy, since substantial SCB contact is most likely detrimental to MCS within the defect or could lead to fibrous tissue formation from large shear strains on exposed native tissue following microfracture surgery. The sutured periosteal flap that is provided during the procedure for ACI most likely provides the implanted chondrocytes protection that does not exist in defects that have undergone microfracture, and thus ACI is more appropriate for larger defects. While there may be a threshold based on defect rim stress, our findings, along with recently published outcomes comparing microfracture and ACI (Knutsen et al., 2004), suggest that SCB contact could be the cause of detrimental interactions with native tissue in defects. These results suggest that a threshold may exist and is a product of SCB contact, rather than defect rim stress. At any rate, SCB contact should be considered when prescribing surgical cartilage restoration procedures, and it should be minimized.

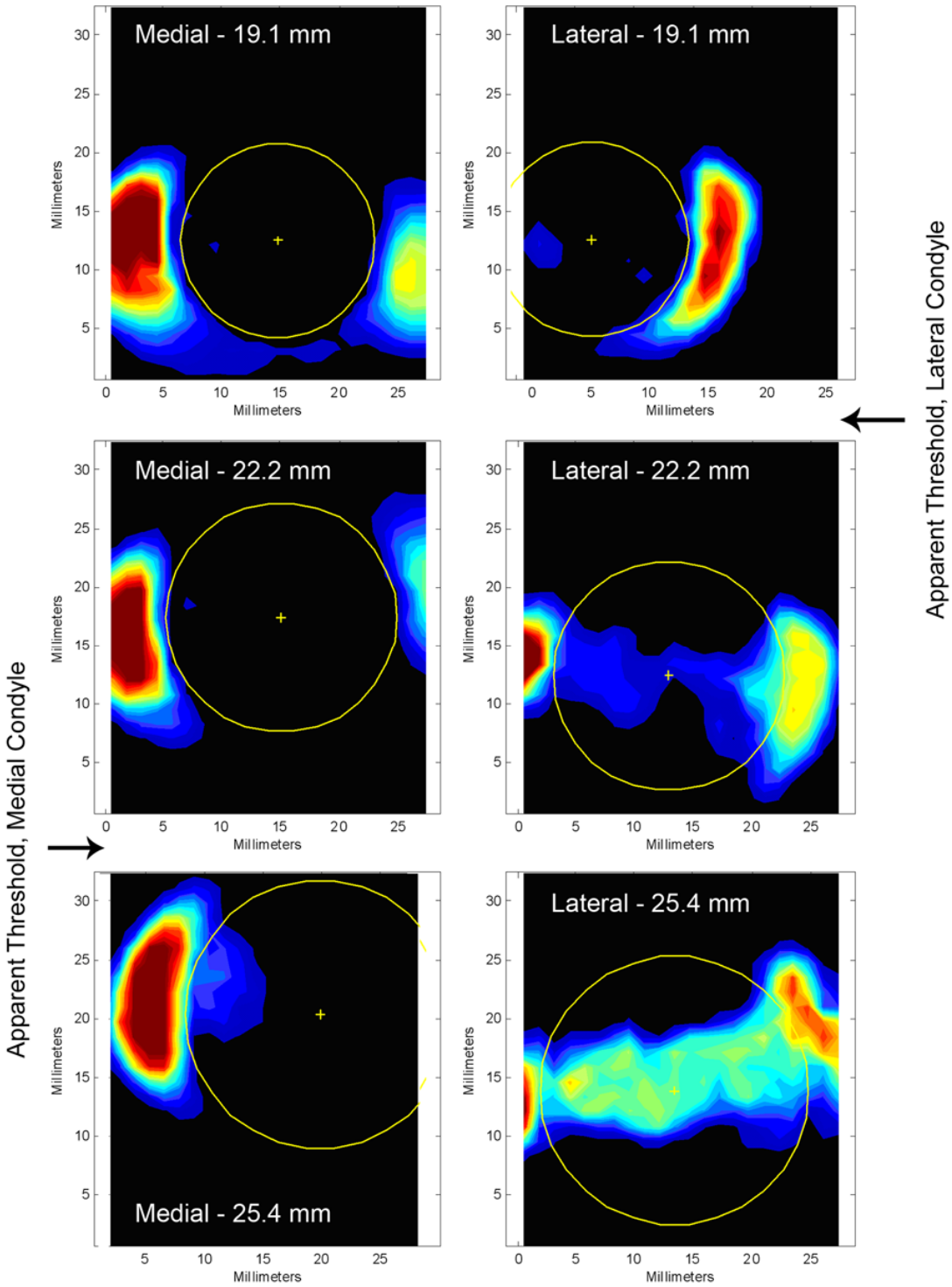

Figure 28: MATLAB Contour Plots of Circular Defects

Measurements from the medial and lateral condyles are on the left and right columns, respectively. Note the increased contact area inside the defect circle (yellow), as defect size increases from top to bottom of figure. Also note the increase in contact area on the lateral side compared to the medial side.

5.2 Medial and Lateral Condyle Differences

In addition, a significant increase in SCB contact was shown in defects occurring on the lateral femoral condyle compared to that of the medial side, and this pattern held for all defect shapes. The apparent SCB contact threshold was more definite when considering medial and lateral defects separately. The data suggested that the largest increase in contact area occurred between 19.1 mm and 22.2 mm for lateral defects but between 22.2 mm and 25.4 mm for medial defects. It was noted that the curvature of the medial and lateral condyles differed significantly. Across all specimens tested, the lateral condyle was characterized by a convex curvature, in contrast to the concave medial condyle. This is also true for the human knee (Figure 29) (Koo and Andriacchi, 2007).

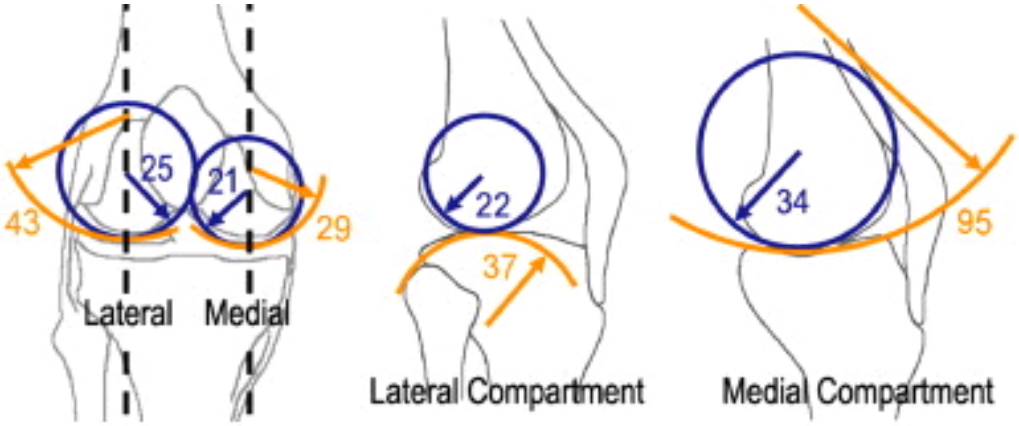

Figure 29: Illustration of Medial and Lateral Differences in the Human Knee
The values show the average values for radii of curvature of 11 subjects in a study by Koo and Andriacchi (2007). Note the convex surfaces contacting in the lateral compartment and the concave/convex surfaces contacting in the medial compartment.

Thus, during loading on the lateral side, the convex femoral condyle and convex tibial condyle consistently led to significant SCB contact in a smaller defect than in the case of the medial side. These results suggest that consideration of the location of a defect may be necessary in choosing an appropriate clinical procedure, as SCB contact was significantly more pronounced and occurred in smaller defects on the lateral condyle.

5.3 Differences in SCB Contact Based on Shape and Orientation

One of the goals of this study was to investigate the effect on SCB contact of varying the shape of defects. The femoral condyle is not a spherical body, as the main radii of curvature in the sagittal and coronal planes are not equal (Figure 30) (Koo and Andriacchi, 2007). We hypothesized that an oval defect oriented in the M-L direction would lead to different contact trends than that of an oval defect oriented in the A-P direction. Our preliminary results supported this hypothesis, as it was determined that the dimension that was the most significant factor in the magnitude of SCB contact area was the M-L dimension, regardless of whether it was the short or long axis dimension (Figure 30).

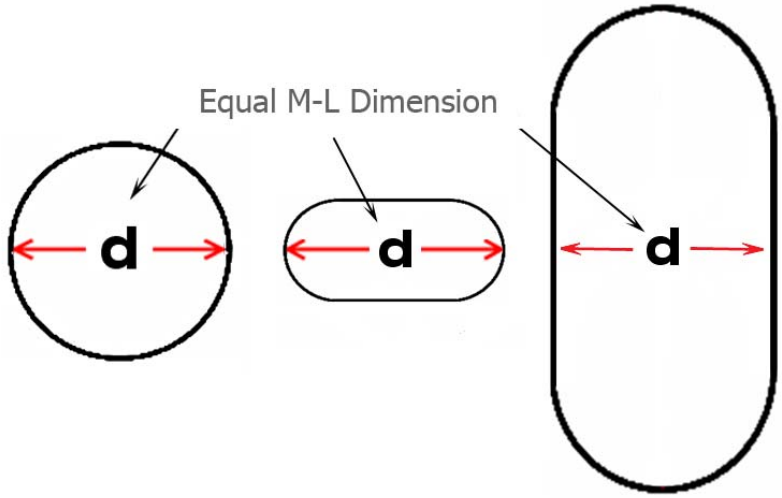

Figure 30: Schematic of Defects with Equal Medial – Lateral Dimensions
Preliminary results suggest that the influential dimension is the medial to lateral dimension when considering SCB contact area.

For example, our results suggest showed that that an oval with a 6.35 mm long axis oriented in the M-L direction will lead to SCB contact that is comparable to that of an oval with a 12.7 mm long axis oriented in the A-P direction. This is because the two defects have equal M-L dimensions (6.35 mm). As the results showed, it was consistently found that defects of equal M-L dimensions were statistically similar, while those which had different

M-L dimensions were statistically different. These findings are can best be explained by the fact that the femoral radius of curvature is smaller, or has more drastic changes in curvature, in the coronal plane. Therefore, the SCB becomes more exposed by widening a defect in the M-L direction than in A-P direction. These findings suggest that the most important dimension for any defect shape is the defect width in the M-L direction.

5.4 Limitations and Shortcomings

While this study has brought to light a number of important aspects of OA progression from focal defects, there are obviously some shortcomings. Our study was based on an quasi-static bovine model of joint loading, the results of which may not be entirely applicable to human clinical situations. This thesis presents a OA progression threshold size for defect, but because of the differences in bovine and human knee geometry and material properties, these results should be viewed as conceptual findings rather than explicit indications for the surgeries discussed. However, it is believed that similar results would be realized in a human cadaver study. Also, because the quasi-static loading used in the study was not representative of physiological loading, the mechanical factors leading to SCB contact may be different in vivo.

The results here were considered with regards to the potential for repair tissue generation in the early stages of microfracture surgery and ACI. However, following these procedures a defect is not empty, but rather it is filled with a fluid-like substance. Therefore, the opposing cartilage surface would not contact subchondral bone without first coming in contact with this pre-cartilage fluid. The resistance from this substance would be minimal, but would still exist.

In order to gain access to the femoral condylar surface, it was necessary to remove the joint capsule and menisci, which would presumably lead to changes in the kinematics and dynamics of the knee during loading.

Finally, in order to secure the joint in the test jigs, the knee specimens tested were not able to rotate or translate during loading. The degrees of freedom allowed by the securing method were not physiologically accurate, which could have produce loading situations that are not experienced in vivo.

Chapter 6: Conclusion

6.1 Contributions

The purpose of this research was to investigate the effects of articular cartilage defect size and shape on subchondral bone contact. Previous research has shown that subchondral bone undergoes changes that are associated with osteoarthritis (Buckland-Wright, 2004; Minas, 1999) and it has also been shown that defect size is a factor in the progression of osteoarthritis (Brown et al., 1991; Convery et al., 1972; Guettler et al., 2004). This study determined that there is likely a link between defect size and subchondral bone contact during loading and a number of clinically relevant conclusions have been made. Our results suggest that subchondral bone contact may be an important factor in osteoarthritis progression and in the existence of a defect progression threshold. Also, our findings suggest that subchondral bone contact is likely dependent on condyle curvature, which should be considered when prescribing surgical procedures. Finally, preliminary results showed that defect shape may also need to be considered.

The findings from this research are applicable to many aspects of articular cartilage

defect repair. We have investigated the effect of various cartilage defect features on subchondral bone contact with the opposing cartilage surface, which can provide insight into clinical decisions about appropriate surgical procedures when information about a specific defect is known. We have also investigated the effect defect shape and orientation on the mechanical environment, which has not been done in the past. We have gained knowledge about the bovine knee, which is frequently used in biomechanical animal studies, regarding its differences and similarities with the human knee. Also, this research provides a basis for future research of similar scope using human knees.

Prior to this study, subchondral bone contact within a defect had not been quantified experimentally. With the use of thin film pressure sensors (Tekscan) and a custom MATLAB script, a novel method for calculating SCB contact area within a defect was introduced.

6.2 Additional Applications and Future Work

The results and conclusions from this study revealed that SCB contact may be an important factor to guide management of focal articular cartilage defects in the knee. However, because the study was based on experimental testing of bovine knees, it is difficult to directly apply the findings to clinical situations, and therefore one of the most obvious extensions of the project would be to replicate the project using human cadaver knees. The results from such a study could be applied more explicitly in an effort to answer the current unanswered questions regarding a defect size threshold.

This study also showed that there was a major increase in SCB contact in defects on the lateral condyle, which is characterized by contacting convex surfaces, as is the case in

humans. Because the study was not specifically investigating the effect of condyle shape on defect SCB contact, there was no quantitative measure of condyle curvature. Thus, a possible future study is to look into the effect of condyle shape and curvature on SCB contact using a similar protocol as the one used for this study.

Because bovine knees are much more readily available and inexpensive than human cadaver knees, it is possible to complete bovine studies much more quickly and easily. There is a problem, though, when attempting to translate results from bovine studies to clinical considerations. A quantitative study of the similarities and differences between bovine and human knees could enhance the results of future bovine studies when attempting to relate them to the human knee.

Static models of the knee provide researchers with valuable information and are usually acceptable to investigate problems. However, a dynamic study of similar scope to this project could provide more useful findings. One such study might look at SCB contact in a defect during continuous passive motion, which is the immediate rehabilitation exercise for both microfracture and ACI. A significant amount of repair tissue generation occurs during CPM rehabilitation, and this is accredited to the mechanical stimulus applied to the defect area. This protocol executed in this study could be adapted to a dynamic study to investigate the measured SCB contact and compressive stresses exhibited in the defect region.

The novel method for calculating SCB contact area in MATLAB using data from the Tekscan software will need to be examined though a validation study. There are plans for this in the near future.

6.3 Summary

This research has presented findings that suggest that defect size is dominant factor in OA progression; as defects become larger subchondral bone contact is increased, leading to a further defect progression. In addition, other factors such as defect shape and condyle location may influence subchondral bone contact. The findings suggest that all of these factors must be accounted for in a clinical algorithm for the management of focal defects.

The mechano-transduction of bone and cartilage cells is an amazing process that enables the human knee to perform functions that would not be possible for a metabolically dormant system. By balancing the synthesis and degradation of chondrocytes, while at the same time monitoring bone growth and resorption, these unidentified cellular sensors respond to forces in the knee so that the healthy knee can provide optimal compression resistance and lubrication. However, focal traumatic defects in the cartilage lead to situations that are detrimental to both the cartilage and subchondral bone, creating a breach in the equilibrium in the knee. Articular cartilage defects progress inevitably when intervention does not take place, with changes in the subchondral bone and deterioration of the cartilage taking place. Furthermore, articular cartilage defect intervention, such as the surgical procedures discussed in this study, may not be successful in halting OA progression if the treated defects are not appropriate for the selected surgical procedure.

BIBLIOGRAPHY

Attur, M.G., Dave, M., Akamatsu, M., Katoh, M. and Amin, R., 2002. Osteoarthritis or osteoarthrosis: the definition of inflammation becomes a semantic issue in the genomic era of molecular medicine. Osteoarthritis and Cartilage, 10: 1-4.

Brown, T., Pope, D., Hale, J., Buckwalter, J. and Brand, R., 1991. Effects of osteochondral defect size on cartilage contact stress. Journal of Orthopaedic Research, 9(4): 559-567.

Buckland-Wright, C., 2004. Subchondral bone changes in hand and knee osteoarthritis detected by radiography. Osteoarthritis and Cartilage(12): S10-S19.

Burks, R.T., Greis, P.E., Arnoczky, S.P. and Scher, C., 2006. The Use of a Single Osteochondral Autograft Plug in the Treatment of a Large Osteochondral Lesion in the Femoral Condyle. The American Journal of Sports Medicine, 35(2): 247-255.

Bush, P.G., Hodkinson, P.D., Hamilton, G.L. and Hall, A.C., 2005. Viability and volume of in situ bovine articular chondrocytesdchanges following a single impact and effects of medium osmolarity. Osteoarthritis and Cartilage, 13: 54-65.

Cameron, M., Briggs, K. and Steadman, J.R., 2003. Reproducibility and Reliability of the Outerbridge Classification for Grading Chondral Lesions of the Knee Arthroscopically. The American Journal of Sports Medicine, 31(1): 83-86.

Carter, D.R., 1987. Mechanical loading history and skeletal biology. Journal of Biomechanics, 20(11-12): 1095-1109.

Carter, D.R., Beaupre, G.S., Giori, N.J. and Helms, J.A., 1998. Mechanobiology of Skeletal Regeneration. Clinical Orthopaedics and Related Research(355S): S41-S55.

Carter, D.R. and Wong, M., 2003. Modelling cartilage mechanobiology. The Philosophical Transactions of the Royal Society(358): 1461-1471.

Convery, F.R., Akeson, W.H. and Keown, G.H., 1972. The Repair of Large Osteochondral Defects. Clinical Orthopaedics and Related Research(82): 253-262.

Drewniak, E., Crisco, J., Spenciner, D. and Fleming, B., 2007. Accuracy of circular contact area measurements with thin-film pressure sensors. Journal of Biomechanics, 40: 2569-2572.

Duda, G. et al., 2001. Chondrocyte Death Precedes Structural Damage in Blunt Impact Trauma. Clinical Orthopaedics and Related Research(393): 302-309.

Felson, D.T., 2006. Osteoarthritis of the Knee. New England Journal of Medicine(354): 841-848.

Flik, K.R., Verma, N., Cole, B.J. and Bach, B.R., 2007. Cartilage Repair Strategies. Articular Cartilage Structure, Biology, and Function. Humana Press, Totowa, NJ.

Garnero, P. et al., 2002. Uncoupling of Type II Collagen Synthesis and Degradation Predicts Progression of Joint Damage in Patients With Knee Osteoarthritis. Arthritis and Theumatism, 46(10): 2613–2624.

Gill, T., Asnis, P. and Berkson, E., 2006. The Treatment of Articular Cartilage Defects Using the Microfracture Surgery. Journal of Orthopaedic & Sports Physical Therapy, 36(10): 728-738.

Guettler, J.H., Demetropoulos, C.K., Yang, K.H. and Jurist, K.A., 2004. Osteochondral Defects in the Human Knee. The American Journal of Sports Medicine, 32(6): 1451-1458.

Harris, M.L., Morberg, P., Bruce, W.J.M. and Walsh, W.R., 1999. An improved method for measuring tibiafemoreal contact areas in total knee arthroplasty: a comparison of K-scan sensor and Fuji film. Journal of Biomechanics, 32: 951-958.

Hinton, R., Moody, R., Davis, A. and Thomas, S., 2002. Osteoarthritis: Diagnosis and Therapeutic Conditions. American Family Physician, 65: 841-848.

Johnson, L., 1986. Arthroscopic abrasion arthroplasty historical and pathologic perspective: present status. Arthroscopy: The Journal of Arthroscopic and Related Surgery, 2(1): 54-69.

Johnson, L., 2001. Clinical Methods of Cartilage Repair: Arthroscopic Abrasion Arthroplasty. Clinical Orthopaedics and Related Research, 391S: S306-S317.

Jones, D. and Peterson, L., 2006. Autologous Chondrocyte Implantation. The Journal of Bone and Joint Surgery, 88: 2501-2520.

Kelly, D.J. and Prendergast, P.J., 2005. Mechano-regulation of stem cell differentiation and tissue regeneration in osteochondral defects. Journal of Biomechanics, 38: 1413-1422.

Knutsen, G., Engebretsen, L., Ludvigsen, T. and Drogset, J., 2004. Autologous Chrondrocyte Implantation

Compared with Microfracture in the Knee: A Randomized Trial. The Journal of Bone and Joint Surgery, 86-A(3): 455-464.
Komistek, R.D., Kane, T.R., Mahfouz, M., Ochoa, J.A. and Dennis, D.A., 2005. Knee mechanics: a review of past and present techniques to determine in vivo loads. Journal of Biomechanics, 38: 215-228.
Koo, S. and Andriacchi, T.P., 2007. A comparison of the influence of global functional loads vs. local contact anatomy on articular cartilage thickness at the knee. Journal of Biomechanics, 40: 2961-2966.
Lewis, P.B., McCarthy, L.P., Kang, R.W. and Cole, B.J., 2006. Basic Science and Treatment Options for Articular Cartilage Injuries. Journal of Orthopaedic & Sports Physical Therapy, 36(10): 717-727.
Loboa, E.G., Beaupre, G.S. and Carter, D.R., 2001. Mechanobiology of initial pseudarthrosis formation with oblique fractures. Journal of Othopaedic Research, 19: 1067-1072.
Mandelbaum, B.R. et al., 1998. Articular Cartilage Lesions of the Knee. The American Journal of Sports Medicine, 26(6): 853-861.
Maquet, P., 1992. Iatrophysics to Biomechanics. The Journal of Bone and Joint Surgery, 74-B: 335-339.
Maroudas, 1976. Balance between swelling pressure and collagen tension in normal and degenerate cartilage. Nature, 260: 808-809.
Minas, T., 1999. The role of cartilage repair techniques, including chondrocyte transplantation, in focal chondral knee damage. AAOS Instructional Course Lectures, 48: 629-643.
Mithoefer, K., Williams, R.J., Warren, R. and Potter, H., 2006. Chondral Resurfacing of Articular Cartilage Defects in the Knee with the Microfracture Technique. The Journal of Bone and Joint Surgery, 87-A: 1911-1920.
Nelson, B., Anderson, D., Brand, R. and Brown, T., 1998. Effect of osteochondral defects on articular cartilage. Contact pressures studied in dog knees. Acta orthopaedica Scandinavica, 59(5): 574-579.
Pauwels, F., 1973. Atlas zur Biomechanik der gesunden und kranken hufte. Springer Verlag, Berlin.
Peat, G. et al., 2006. Clinical classification criteria for knee osteoarthritis: performance in the general population and primary care. Annals of Rheumatory Disease(65): 1363-1367.
Pena, E., Calvo, M., Martinez, M. and Doblaré, M., 2007. Effect of the size and location of osteochondral defects in degenerative arthritis. A finite element simulation Computers in Biology and Medicine, 37(3): 367-387.
Radin, E., Paul, I. and Lowy, M., 1970. A Comparison of the Dynamic Force Transmitting Properties of Subchondral Bone and Articular Cartilage. The Journal of Bone and Joint Surgery, 52: 444-456.
Riegger-Krugh, C., McCarthy, E., MRobinson, M. and Wegzyn, D., 2008. Autologous Chondrocyte Implantation: Current Surgery and Rehabilitation. Medicine & Science In Sports & Excercise, 40(2): 206-214.
Sandell, L.J. and Aigner, T., 2001. Articular cartilage and changes in arthritis. An introduction: Cell biology of osteoarthritis. Arthritis Research, 3: 107-113.
Setton, L.A., Elliot, D.M. and Mow, V.C., 1999. Altered mechanics of cartilage with osteoarthritis: humanosteoarthritis and an experimental model of joint degeneration. Osteoarthritis and Cartilage(7): 2-14.
Sgaglione, N., Miniaci, A., Gillogly, S. and Carter, T., 2002. Update on Advanced Surgical Techniques in the Treatment of Traumatic Focal Articular Cartilage Lesions in the Knee. Arthroscopy: The Journal of Arthroscopic and Related Surgery, 18(2): 9-32.
Shapiro, F., 1993. Osteopetrosis: Current Clinical Considerations. Clinical Orthopaedics and Related Research(294): 34-44.
Steadman, J.R., Rodkey, W.G. and Rodrigo, J.L., 2001. Microfracture: Surgical Technique and Rehabilitation to Treat Chondral Defects. Clinical Orthopaedics and Related Research(391S): S362-S369.
van der Meulen, M. and Huickes, R., 2002. Why mechanobiology? A survey article. Journal of Biomechanics, 35: 401-414.
Wraighte, P. and Scammell, B., 2006. Principles of fracture healing. Sugery, 24(6): 198-207.
Yen, Y.M., Cascio, B. and O'Brien, L., 2008. Treatment of Osteoarthritis of the Knee with Microfracture and Rehabilitation. Medicine and Science In Sports & Excercise, 40(2): 200-205.

APPENDIX A

Dimensional Data of Knees

Knee No.	Defect Group	L/R	Condylar Width (mm)		Condylar Depth (mm)		Cartilage Thickness (mm)		Angle (deg. val.)
			Medial	Lateral	Medial	Lateral	Medial	Lateral	
1	circle	L	45	42.5	53.8	58.3	0.69	0.8525	2
2	circle	R	43.4	40.8	59.3	62.4	0.8475	0.9625	2.5
3	circle	L	53.4	42.6	65.9	67.3	1.0675	1	5
5	circle	L							
7	oval AP	L	46.4	44.7	65.5	70.4	1.0075	0.84	5
9	oval AP	L	54.7	48.2	69.9	69.3	1.3075	1.0575	1
12	oval AP	R	46.6	43.3	53.6	57.9	0.885	0.7625	4.5
14	oval AP	L	55.1	53.5	76.9	86	0.99	1.22	4.5
16	oval ML	R	52.3	54.6	74.9	73.6	0.9625	0.815	1.5
17	oval ML	L	50.7	53.1	64.7	73.5	1.1275	1.145	6.5
18	oval ML	L	53.5	48.4	64.4	63.6	1.065	0.995	4.4
19	oval ML	R	51.6	54.1	68.1	66.2	0.965	1.12	8
20	circle	L	54.6	46.2	69.6	65.6	1.0125	1.2025	4
21	circle	L	49.2	44	57.5	66.2	0.745	0.745	3.5

APPENDIX B

MATLAB Code for Calculating Circular Defect Contact Area

```
% contact_area.m

% Uses Tekscan data to calculate the contact area within a circular defect
% region identified by the user

clear all
clc

dat = input('Type the filename with extension, with single quotes around
it:  ');
tekscan(dat)

data_L = data(1:26,1:22);
data_R = data(1:26,43:64);

%% Sensor information

sensor_width = 28; %mm
sensor_height = 33; %mm
sensels_per_width = 22;
sensels_per_height = 26;
sensel_width = sensor_width/sensels_per_width; %mm
sensel_height = sensor_height/sensels_per_height; %mm

%% Position matrices - create 26x22 matrices of position

pos_x_row = sensel_width/2:sensel_width:sensor_width-sensel_width/2;
for i = 1:26
    pos_x(i,:) = pos_x_row;
end
pos_x = 28-pos_x;
pos_y_column = [sensel_height/2:sensel_height:sensor_height-
sensel_height/2]';
for j = 1:22
    pos_y(:,j) = pos_y_column;
end

rad = .5*((input('Type the defect diameter in mm:  '))-1.27*2);
display('A plot will appear.  Click on the center of the defect.')

%% Execute file for the plot on the left

%Define black as the color for zero
map = colormap('jet'); map(1,3)=0;colormap(map);

figure(1)
contour3(pos_x,pos_y,data_L,30,'LineStyle','none')
title('Contact Pressure Plot of Left Sensor')
xlabel('Millimeters')
```

```
ylabel('Millimeters')
axis equal
[click_xL,click_yL] = ginput(1);

% Calculate equation for the circle created by the radius input and the
centerpoint
theta = 0:2*pi/30:2*pi;
cir_x = rad*cos(theta)+click_xL;
cir_y = rad*sin(theta)+click_yL;

% Plot again, with the circle displayed

figure(1)
contourf(pos_x,pos_y,data_L,30,'LineStyle','none')
title('Contact Pressure Plot of Left Sensor')
xlabel('Millimeters')
ylabel('Millimeters')
hold on
plot(cir_x,cir_y,'--y',click_xL,click_yL,'+y','LineWidth',2)
axis equal
hold off
yn = 0;
yn = input('Is this right?  Type 1 for yes and 0 for no:  ');
while yn == 0
    [click_xL,click_yL] = ginput(1);
    cir_x = rad*cos(theta)+click_xL;
    cir_y = rad*sin(theta)+click_yL;
    figure(1)
    contourf(pos_x,pos_y,data_L,30,'LineStyle','none')
    title('Contact Pressure Plot of Left Sensor')
    xlabel('Millimeters')
    ylabel('Millimeters')
    hold on
    plot(cir_x,cir_y,'--y',click_xL,click_yL,'+y','LineWidth',2)
    axis equal
    hold off
    yn = input('Is this right?  Type 1 for yes and 0 for no:  ');
end

% Determine area

pos_x_cen = pos_x-click_xL;
pos_y_cen = pos_y-click_yL;

[ht,wd] = size(data_L);
yn_mat_L = zeros(26,22);
for i = 1:ht
    for j = 1:wd
        rad_pos(i,j) = sqrt(pos_x_cen(i,j)^2+pos_y_cen(i,j)^2);
        if rad_pos(i,j)>=rad
            rad_pos(i,j)=0;
        else
            yn_mat_L(i,j) = rad_pos(i,j)/rad_pos(i,j);
        end
        if data_L(i,j)>0
```

```
            cp_yn_L(i,j)=1;
        else
            cp_yn_L(i,j)=0;
        end
    end
end

% Determine if the indices are within the circle and have contact
area_y_n_L = yn_mat_L.*cp_yn_L;

sensel_area = sensel_width*sensel_height;
contact_area_left = 0;
column_total = 0;
for i = 1:wd
    column_sum = sum(area_y_n_L(:,i));
    column_total = column_sum+column_total;
    contact_area_left = sensel_area*(column_sum)+contact_area_left;
end


%% Execute file for the plot on the right


figure(2)
contourf(pos_x,pos_y,data_R,30,'LineStyle','none')
title('Contact Pressure Plot of Right Sensor')
xlabel('Millimeters')
ylabel('Millimeters')
axis equal
[click_xR,click_yR] = ginput(1);

% Calculate equation for the circle created by the radius input and the
centerpoint
theta = 0:2*pi/30:2*pi;
cir_x = rad*cos(theta)+click_xR;
cir_y = rad*sin(theta)+click_yR;

% Plot again, with the circle displayed

figure(2)
contourf(pos_x,pos_y,data_R,30,'LineStyle','none')
title('Contact Pressure Plot of Right Sensor')
xlabel('Millimeters')
ylabel('Millimeters')
hold on
plot(cir_x,cir_y,'--y',click_xR,click_yR,'+y','LineWidth',2)
axis equal
hold off
yn = 0;
yn = input('Is this right?  Type 1 for yes and 0 for no:  ');
while yn == 0
    [click_xR,click_yR] = ginput(1);
    cir_x = rad*cos(theta)+click_xR;
    cir_y = rad*sin(theta)+click_yR;
```

```
    figure(2)
    contourf(pos_x,pos_y,data_R,30,'LineStyle','none')
    title('Contact Pressure Plot of Right Sensor')
    xlabel('Millimeters')
    ylabel('Millimeters')
    hold on
    plot(cir_x,cir_y,'--y',click_xR,click_yR,'+y','LineWidth',2)
    axis equal
    hold off
    yn = input('Is this right?  Type 1 for yes and 0 for no:  ');
end

% Determine area

pos_x_cen = pos_x-click_xR;
pos_y_cen = pos_y-click_yR;

[ht,wd] = size(data_R);
yn_mat_R = zeros(26,22);
for i = 1:ht
    for j = 1:wd
        rad_pos(i,j) = sqrt(pos_x_cen(i,j)^2+pos_y_cen(i,j)^2);
        if rad_pos(i,j)>=rad
            rad_pos(i,j)=0;
        else
            yn_mat_R(i,j) = rad_pos(i,j)/rad_pos(i,j);
        end
        if data_R(i,j)>0
            cp_yn_R(i,j)=1;
        else
            cp_yn_R(i,j)=0;
        end
    end
end

% Determine if the indices are within the circle and have contact

area_y_n_R = yn_mat_R.*cp_yn_R;

sensel_area = sensel_width*sensel_height;
contact_area_right = 0;
column_total = 0;
for i = 1:wd
    column_sum = sum(area_y_n_R(:,i));
    column_total = column_sum+column_total;
    contact_area_right = sensel_area*(column_sum)+contact_area_right;
end
cont_area = [contact_area_left contact_area_right];
display('The calculated area of the left side is:')
display(contact_area_left);
display('The calculated area of the right side is:')
display(contact_area_right);
```